Structural Insights into Monoamine Oxidase Inhibitory Potency and Selectivity of 7-Substituted Coumarins from Ligand- and Target-Based Approaches

Marco Catto,[†] Orazio Nicolotti,[†] Francesco Leonetti,[†] Andrea Carotti,[†] Angelo Danilo Favia,[†] Ramón Soto-Otero,[‡] Estefanía Méndez-Álvarez,[‡] and Angelo Carotti*,[†]

Dipartimento Farmaco-Chimico, Università di Bari, Via Orabona 4, 70125 Bari, Italy, and Grupo de Neuroquímica, Departamento de Bioquímica y Biología Molecular, Facultad de Medicina, Universidad de Santiago de Compostela, Santiago de Compostela, Spain

Received February 16, 2006

A new series of 3-, 4-, 7-polysubstituted coumarins have been designed and evaluated for their monoamine oxidase A and monoamine oxidase B (MAO-A and MAO-B) inhibitory potency. Substituents at position 7 consisted of a bridge of different physicochemical nature linking a phenyl ring to the coumarin scaffold. Structure−affinity and structure−selectivity relationships, derived through CoMFA-GOLPE and docking studies, revealed the key physicochemical interactions responsible for the observed MAO-B and MAO-A inhibitory potency and suggested the main structural determinants for high selectivity toward one of the two enzymatic isoforms. The predictive power of our models was proved with the design of a new inhibitor demonstrating an outstanding MAO-B affinity ($pIC_{50} = 8.29$) and the highest MAO-B selectivity ($\Delta pIC_{50} = 3.39$) within the entire series of ligands examined herein.

Introduction

Monoamine oxidase (MAO; EC 1.4.3.4, amine−oxygen oxidoreductase) is a membrane-bound, FAD(FMN)-containing enzyme involved in the oxidative deamination of exogenous and endogenous amines, including neurotransmitters.[1] MAO exists as two distinct enzymatic isoforms, MAO-A and MAO-B,[2,3] which differ in amino acid sequence, substrate specificity, sensitivity to inhibitors, and tissue distribution.[4] MAO-A preferentially deaminates the neurotransmitters serotonin, norepinephrine, and epinephrine and is selectively inhibited by clorgyline, whereas MAO-B acts preferentially on β-phenethylamines and sterically hindered amines and is selectively inhibited by selegiline (L-deprenyl)[5] (Chart 1).

MAO became a neuropharmacological target in the late 1950s with the discovery of the antidepressant properties of MAO inhibitors (MAOIs), such as iproniazid and tranylcypromine (Chart 1). Lack of selectivity, irreversible mechanism of action, severe hepatotoxicity, and even fatal hypertensive crisis of the first-generation MAOIs stimulated further research aimed at the discovery of new, more selective, and less toxic drugs.[6] Several selective MAO-A inhibitors (MAO-AIs), acting as antidepressants (brofaromine, clorgyline, moclobemide and toloxatone), and selective MAO-B inhibitors (MAO-BIs), used alone or in combination with L-Dopa in the therapy of Parkinson's disease (i.e., selegiline and rasagiline,[5,7,8] Chart 1), were discovered. The pronounced neuroprotective effect of selegiline and other selective MAO-BIs in animal models suggested their possible application in the symptomatic treatment of Alzheimer's disease.[9]

The most clinically relevant MAOIs belong to the class of propargylamines, which share a common mechanism of action implying the formation of a covalent bond with the flavin ring of the FAD cofactor.[5]

Although significant advances in the design of selective MAOIs have been achieved in the past 2 decades, a veritable breakthrough in the field occurred only few years ago with the resolution of the X-ray crystal structure of human MAO-B (hMAO-B)[10] and rat MAO-A (rMAO-A).[11] The high-resolution 3D structure of the hMAO-B in complex with a large number of selective inhibitors, covalently bound to the FAD cofactor,[10] finally paved the way to the structure-based design of new modulators of MAO-B activity. More recently, the X-ray crystallographic structure of hMAO-A, covalently bound to the MAO-A selective inhibitor clorgyline, has been reported.[12] As a result, a direct comparison of the binding modes of selective MAOIs was made possible with the potential for a structure-based design of new, more potent and selective hMAOIs. Moreover, a recently published method for screening large series of MAOIs on cloned hMAO-B[13] (for cloned hMAO-A, a similar approach is being developed by the same research groups) should be particularly helpful for a more efficient and rapid discovery of novel MAOIs, since accumulating evidence has shown that inhibition data from rMAOs (the most used source of MAOs) often strongly differ from data collected with similar methods from human enzymes.[14,15]

Following an initial study on the mechanisms of neurotoxication of 1-methyl-4-phenyl-1,2,3,6-tetrahydropyridine (MPTP) by MAO-B,[16] we recently carried out a series of 2D- and 3D-QSAR studies of condensed (di)azines,[17] geiparvarins,[18] and coumarins,[19,20] generally acting as strong and selective MAO-BIs. As for the last class of compounds, we prepared and tested a very large array of inhibitors, which also proved to be potent and selective MAO-BIs.[19,20] Moreover, some of them showed an interesting additional inhibitory activity toward acetylcholinesterase (AChE).[21]

Beginning with these findings and keeping in mind all the relevant structural information on MAOs, we designed other structural variations on coumarins to explore in more detail the structure−affinity and structure−selectivity relationships (SAFIRs and SSRs, respectively) for in vitro MAO inhibition.

Our previous investigations[19,20] highlighted significant changes in MAO-B inhibitory potency and MAO-B/MAO-A (from here on B/A) selectivity arising from the introduction of diverse substituents at position 7. However, given that only few such structural modifications have been made, we decided to expand

* To whom correspondence should be addressed. Phone: +39 080 544-2782. Fax: +39 080 544-2230. E-mail carotti@farmchim.uniba.it.
[†] Università di Bari.
[‡] Universidad de Santiago de Compostela.

10.1021/jm060183l CCC: $33.50
Published on Web 07/07/2006

Chart 1. Chemical Structures of Nonselective and Selective MAO-A (A) and MAO-B (B) Inhibitors

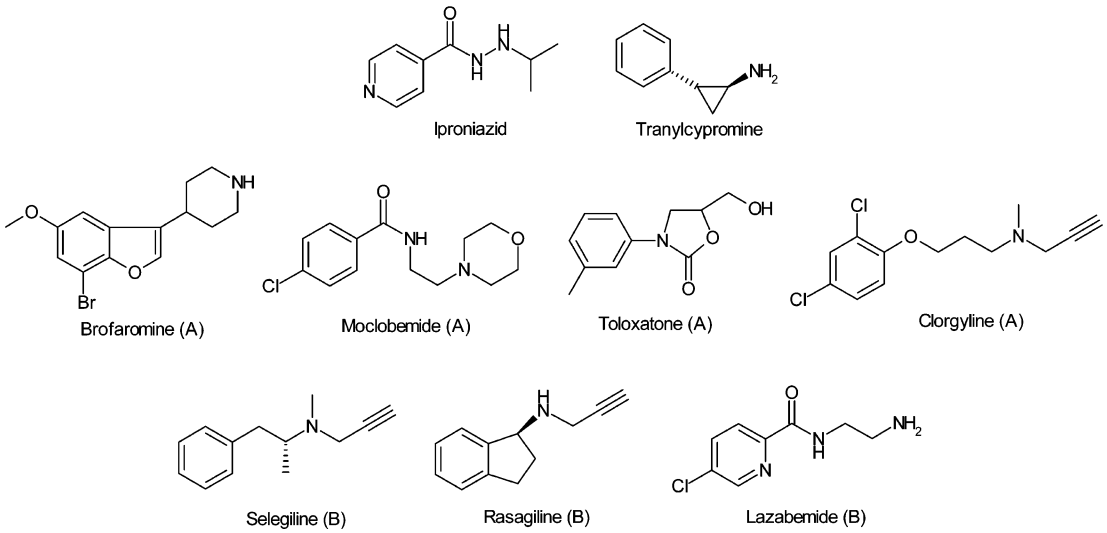

the investigation of the SAFIRs and SSRs through the synthesis and in vitro biological evaluation of a novel series of 7-substituted coumarin derivatives. The substituents at position 7 consist of a phenyl ring linked to a coumarin core by bridges of different size, length, and lipophilic and electronic nature. Along with the newly prepared coumarin derivatives (i.e., compounds **8**, **15**−**17**, **21**, **22**, **27**, **29**, (±)-**31**, (−)-**31**, (+)-**31**, **33**, **36**, and **37**, Table 1), other previously reported 7-substituted coumarins, with no, one, or two methyl groups in position 3 or 4 were considered for a more complete analysis.

Chemistry

The synthesis of many novel coumarin derivatives was performed starting from commercial 7-hydroxycoumarin (umbelliferone, **1**) and previously reported 3,4-dimethyl-7-hydroxycoumarin (**2**),[19] 7-amino-3,4-dimethylcoumarin (**3**),[22] and 7-(bromomethyl)coumarin (**4**)[19] (Chart 2).

3-Methylcoumarin derivative **8** was prepared, according to the pathway reported in Scheme 1, from 7-hydroxy-3-methylcoumarin **5**, prepared in turn from 2,4-dihydroxybenzaldehyde, and benzyl bromide in refluxing ethanol.

Phenyl sulfonate **15** was prepared by reacting 7-hydroxycoumarin (**1**) with benzenesulfonyl chloride in pyridine. Benzoate **16** was obtained from benzoic acid and 7-(bromomethyl)-coumarin (**4**), following a standard synthetic procedure. β-Phenethyl derivative **17** was synthesized from styryl derivative **18**[19] (Table 1) by catalytic hydrogenation over activated platinum on carbon.

Diazotization of 7-aminocoumarin derivative **3**[22] with sodium nitrite in hydrochloric acid, followed by the nucleophilic substitution with sodium benzylmercaptide, yielded thioether **21**, which afforded sulfone **22** upon oxidation with potassium permanganate (Scheme 2).

Sulfonamido derivative **27** was prepared by N-methylation of the already reported 3,4-dimethyl-7-(4-tolylsulfonamido)-coumarin[19] with iodomethane in DMF.

7-Phenoxycoumarin derivative **29** was prepared according to the classical von Pechmann procedure by heating 3-phenoxyphenol and ethyl 2-methylacetoacetate with acid catalysis (Scheme 3).

Racemic benzyl alcohol **31** was obtained by reduction of the phenone derivative **30**[20] with lithium aluminum hydride in THF. The enantiomeric resolution of the racemic mixture of **31** was performed by preparative HPLC on a Chiralcel OD column.

Table 1. MAO-A and -B Inhibitory Activities of Coumarin Derivatives **6**−**43**

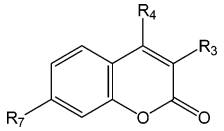

				pIC$_{50}$		
compd	R_3	R_4	R_7	MAO-A	MAO-B	ΔpIC$_{50}$[g]
6[a]	H	H	$OCH_2C_6H_5$	5.17	7.26	2.09
7[a]	H	CH_3	$OCH_2C_6H_5$	5.71	7.74	2.03
8	CH_3	H	$OCH_2C_6H_5$	5.26	8.18	2.92
9[a]	CH_3	CH_3	$OCH_2C_6H_5$	6.16	8.36	2.20
10[a]	H	H	$CH_2OC_6H_5$	6.41	7.07	0.66
11[a]	H	H	$CH_2NHC_6H_5$	4.38	5.67	1.29
12[b]	H	H	$CH_2SC_6H_5$	5.42	5.89	0.47
13[b]	H	H	$CH_2S(O)C_6H_5$	5.21	6.24	1.03
14[b]	H	H	$CH_2S(O_2)C_6H_5$	4.66	4.59	−0.07
15	H	H	$OS(O_2)C_6H_5$	6.35	4.26	−2.09
16	H	H	$CH_2OC(O)C_6H_5$	5.02	5.62	0.60
17	CH_3	CH_3	$CH_2CH_2C_6H_5$	5.15	6.34	1.19
18[a]	CH_3	CH_3	tCH=CHC_6H_5	6.39	7.55	1.16
19[a]	CH_3	CH_3	$NHCH_2C_6H_5$	5.80	6.79	0.99
20[a]	CH_3	CH_3	$NHC(O)C_6H_5$	5.86	6.72	0.86
21	CH_3	CH_3	$SCH_2C_6H_5$	5.00	7.40	2.40
22	CH_3	CH_3	$S(O_2)CH_2C_6H_5$	4.73	5.56	0.83
23[a]	CH_3	CH_3	$OS(O_2)C_6H_5$	7.12	5.28	−1.84
24[a]	CH_3	CH_3	$OS(O_2)$−4′-CH_3−C_6H_4	7.33	4.50[f]	−2.83
25[a]	CH_3	CH_3	$OS(O_2)$−4′-NO_2−C_6H_4	7.90	4.77	−3.13
26[a]	CH_3	CH_3	$OS(O_2)$−4′-OCH_3−C_6H_4	7.15	5.00	−2.15
27	CH_3	CH_3	$N(CH_3)S(O_2)$−4′-$CH_3C_6H_4$	5.34	4.50[f]	−0.84
28[a]	CH_3	CH_3	$OCH(CH_3)C_6H_5$	5.45	6.49	1.04
29	CH_3	CH_3	OC_6H_5	4.50[f]	5.49	0.99
30[b]	CH_3	CH_3	$OCH_2C(O)C_6H_5$	5.01	7.74	2.73
(±)-31	CH_3	CH_3	$OCH_2CH(OH)C_6H_5$	5.00	7.15	2.15
(−)-31	CH_3	CH_3	$OCH_2CH(OH)C_6H_5$	5.49	6.52	1.03
(+)-31	CH_3	CH_3	$OCH_2CH(OH)C_6H_5$	5.00	7.55	2.55
32[a]	CH_3	CH_3	$OCH_2CH_2C_6H_5$	6.00	8.25	2.25
33	CH_3	CH_3	$OCH_2CH_2OC_6H_5$	4.99	7.57	2.58
34[c]	CH_3	CH_3	$OCH_2CH_2CH_2C_6H_5$	4.64	7.28	2.64
35[d]	CH_3	CH_3	$OS(O_2)CH_2C_6H_5$	5.70	4.00[f]	−1.70
36	CH_3	CH_3	$OCH_2S(O_2)C_6H_5$	5.55	6.06	0.51
37	CH_3	CH_3	OCH_2-tCH=CHC_6H_5	4.50[f]	6.95	2.45
38[e]	H	H	OCH_2-tCH=CHC_6H_5	4.00[f]	7.24	3.24
39[a]	CH_3	CH_3	OCH_2−3′-F−C_6H_4	6.24	8.55	2.31
40[a]	CH_3	CH_3	OCH_2−3′-Cl−C_6H_4	5.95	8.48	2.53
41[a]	CH_3	CH_3	OCH_2−3′,4′-F_2−C_6H_3	6.91	8.94	2.03
42[a]	CH_3	CH_3	OCH_2−3′,5′-F_2−C_6H_3	6.17	8.52	2.35
43	CH_3	H	OCH_2−3′-Cl−C_6H_4	4.90	8.29	3.39

[a] From ref 19. [b] From ref 20. [c] From ref 42. [d] From ref 43. [e] From ref 44. [f] Truncated value estimated from the percent of inhibition at two different concentrations. [g] ΔpIC$_{50}$ is the difference between pIC$_{50}$ of MAO-B and pIC$_{50}$ of MAO-A.

Compounds **33**, **36**, and **37** were synthesized from 3,4-dimethyl-7-hydroxycoumarin (**2**) by nucleophilic substitution

Chart 2. Starting Coumarin Derivatives

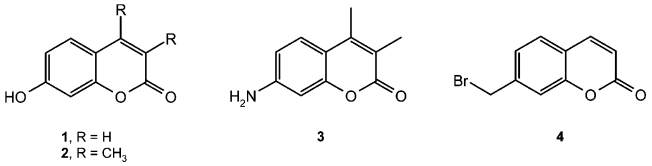

1, R = H
2, R = CH_3 **3** **4**

Scheme 1[a]

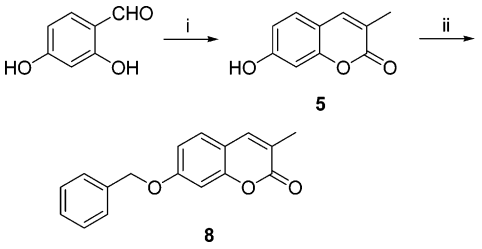

5 **8**

[a] Reaction conditions: (i) CH_3CH_2COONa, $(CH_3CH_2CO)_2O$, piperidine, Δ; (ii) benzyl bromide, K_2CO_3, EtOH, Δ.

Scheme 2[a]

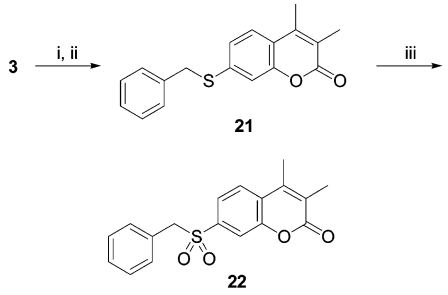

21 **22**

[a] Reaction conditions: (i) $NaNO_2$, HCl; (ii) benzylmercaptan sodium salt; (iii) $KMnO_4$, AcOH, Δ.

Scheme 3[a]

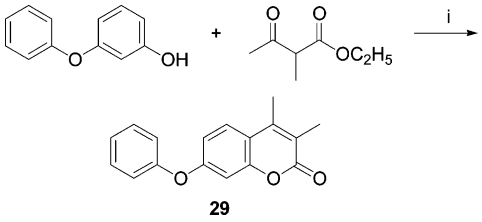

29

[a] Reaction conditions: (i) H^+, Δ.

Scheme 4[a]

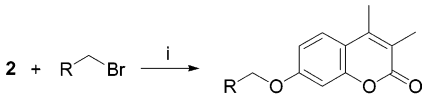

33, R = $CH_2OC_6H_5$
36, R = $S(O_2)C_6H_5$
37, R = *trans*-$CH{=}CHC_6H_5$

[a] Reaction conditions: (i) K_2CO_3, DMF, Δ.

with appropriate bromoalkyl derivatives in DMF and potassium carbonate as an acid scavenger (Scheme 4).

Results and Discussion

The chemical structures of MAOIs examined in this report are shown in Table 1, along with their in vitro inhibitory potencies and B/A selectivity. MAO inhibitory activities were determined on rat brain mitochondria using a continuous spectrophotometric assay based on the monitoring of the oxidation rate of the nonselective, nonfluorescent MAO substrate kynuramine to the fluorescent 4-hydroxyquinoline.[51]

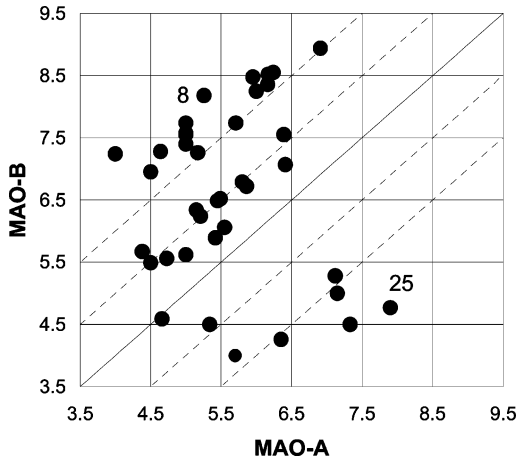

Figure 1. Square plot of rMAO affinity (pIC_{50}) and selectivity. Top-left and bottom-right corners contain inhibitors with high selectivity toward rMAO-B and rMAO-A isoenzymes, respectively. Two of the most potent and selective inhibitors of each enzymatic isoform are highlighted.

To avoid the loss of important information for comparative molecular field analysis (CoMFA), estimated pIC_{50} ($-\log IC_{50}$) values were used for those few inhibitors (see footnote f in Table 1) whose low solubility did not permit the determination of the IC_{50}. ΔpIC_{50}, that is, the difference between pIC_{50} of MAO-B and pIC_{50} of MAO-A, was used as a measure of B/A selectivity in CoMFA. For a more immediate and efficient analysis of the variation of both affinity and selectivity, inhibition data are presented in Figure 1 as a plot of pIC_{50} of MAO-A (x-axis) versus pIC_{50} of MAO-B (y-axis) using the same scale and range for both axes (square plot). Thus, compounds with equal affinities at both isoenzymes lie on the bisector ($y = x$) of this plot, whereas MAO-A or MAO-B selective inhibitors are situated below or above the bisector, respectively. The distance of their pIC_{50} values from the bisector is a direct measure of their degree of selectivity. Four parallel lines were traced at one ΔpIC_{50} unit distance above and below the bisector to enable a straightforward location of inhibitors with an IC_{50}(MAO-A)/IC_{50}(MAO-B) affinity ratio (selectivity) higher than 10 and 100 (i.e., $\Delta pIC_{50} > 1$ and $\Delta pIC_{50} > 2$, respectively). Inhibitors endowed with both high MAO-A affinity and A/B selectivity (i.e., **25**) are located in the lowest right-hand corner of the plot, whereas inhibitors with both high MAO-B affinity and B/A selectivity (i.e., **8**) are located in the upper left-hand corner. At a first glance, the plot suggests that very potent and selective MAO-B inhibitors are more represented in the analyzed set and that no apparent relationship exists between MAO-A and MAO-B affinities.

In a previous report,[19] a significant increase of MAO-B inhibitory affinity of 7-benzyloxycoumarin lead **6** was observed by introducing methyl groups at positions 4 and 3,4 (compounds **7** and **9**, respectively) and introducing the fluorine (**39**) or chlorine (**40**) atom at the meta position of the benzyloxy ring of **9**. We have now prepared the 3-methyl regioisomer of **7** (**8**), which displayed significantly higher MAO-B affinity and B/A selectivity: $pIC_{50} = 8.18$ vs 7.74; $\Delta pIC_{50} = 2.92$ vs 2.03. Moreover, compared to the 3,4-dimethyl congener **9**, 3-methyl derivative **8** exhibited close MAO-B affinity ($pIC_{50} = 8.18$ vs 8.36) and significantly higher selectivity ($\Delta pIC_{50} = 2.92$ vs 2.20). These important findings suggested a straightforward access to highly potent and more selective MAO-B inhibitors.

The substitution of both hydrogens at positions 3 and 4 with methyl groups led to an almost 10-fold increase in MAO-B and

MAO-A inhibitory activities (compare **9** vs **6**, **23** vs **15**), with the only exception being the cinnamyl derivatives (**37** vs **38**).

Isosteric variations of the oxymethylene linker in reference compound **6** led to inhibitors **10**−**12**, all endowed with lower MAO-B affinity and B/A selectivity. Similar isosteric changes on the 3,4-dimethyl lead compound **9** afforded similar results for phenethyl (**17**) and benzylamino (**19**) derivatives, whereas a decrease of MAO-B affinity (pIC_{50} = 7.55 vs 8.36) associated with a slight increase of MAO-A affinity (pIC_{50} = 6.39 vs 6.16) was observed for *trans*-styryl derivative **18**. Interestingly, the thiobenzyl derivative **21** showed a B/A selectivity higher than isoster lead compound **9** (ΔpIC_{50} = 2.40 vs 2.20) as a result of a stronger diminution of the MAO-A affinity (pIC_{50} = 6.16−5.00).

The influence of the linker's length on MAO affinity was assessed by preparing either lower (**29**) or higher (**32** and **34**) homologues of lead compound **9**, as well as the dioxoethylene (**33**) and the cinnamyl (**37**) derivatives. Phenoxy derivative **29** showed a dramatic decrease of affinity at both MAO isoenzymes, while the ethoxy derivative **32** fully retained the activity profile of reference ligand **9**. Further elongation of the bridge with a methylene (**34**) or an oxygen atom (**33**) decreased MAO-B and, to a higher degree, MAO-A affinity, yielding less potent but highly MAO-B selective inhibitors. Interestingly, the long but more rigid cinnamyl derivative **38** displayed MAO affinity values very similar to those of the corresponding hydrogenated analogue **34**.

The oxidation of thioether **12** to sulfone **14** induced a strong decrease of MAO-B affinity and, consequently, B/A selectivity. The same transformation performed on homologous thioether **21** afforded sulfone **22**, which presented very poor affinities for both MAO isoenzymes. The oxidation of thioether **12** to sulfoxide **13** restored satisfactory MAO-B affinity and B/A selectivity.

The biological evaluation of new sulfonic ester **15** confirmed the inversion of selectivity already observed in the corresponding homologue **23**.[19,23] This effect was even more pronounced in the para-substituted phenyl sulfonates **24**−**26** reported in our previous paper.[19] The affinity and selectivity of other newly synthesized sulfonyl-containing inhibitors, such as *N*-methyltolylsulfonamide **27** and benzylsulfonate **35**, demonstrate that an intact sulfonate group, directly linked to the coumarin ring, is a key structural requisite for high A/B selectivity. A further support to this general rule was given by sulfone **22**, which exhibited an inverted B/A selectivity compared to the isosteric sulfonate **23** (ΔpIC_{50} = 0.83 vs −1.84).

To further evaluate the modulation of affinity arising from the introduction of polar oxygenated groups in the bridge, benzoate (**16**) and phenone (**30**) derivatives were prepared. Compound **30**, the only ketonic derivative in the entire series, displayed quite high MAO-B affinity and B/A selectivity. Compound **16** was endowed with an affinity in the micromolar range at both enzyme isoforms. It must be remembered that benzoate **16** could be partly hydrolyzed during the inhibition assay. This might explain the unexpectedly high drop of affinity compared to more stable inhibitors with similar structural features.

Finally, the effect of branching in the bridge on MAO affinity was studied with the synthesis of ethoxy derivative **28**[19] and alcohol **31**. The introduction of the methyl group on the bridge of compound **9** leading to **28** determined a remarkable decrease of MAO-B affinity (about 2 orders of magnitude), and as a consequence, B/A selectivity strongly decreased (ΔpIC_{50} = 1.04 vs 2.20). A similar, but less intense, effect was observed with the introduction of a hydroxyl group in the bridge at position 7 affording alcohol **31**. To verify whether an enantioselective interaction might occur at the enzyme binding sites with the benzylic hydroxyl, the racemic mixture of **31** was resolved through preparative chiral HPLC and the two enantiomers were tested individually. The (+)-enantiomer revealed higher MAO-B affinity and slightly lower MAO-A affinity than (−)-enantiomer. This determined a significantly enhanced B/A selectivity (ΔpIC_{50} = 2.55 vs 1.03) and suggested a possible enantioselective interaction of the benzyl alcohol moiety at the MAO-B binding site. Additional studies are warranted for a complete comprehension of the enantioselective interactions of polar substituents placed on the bridge at position 7.

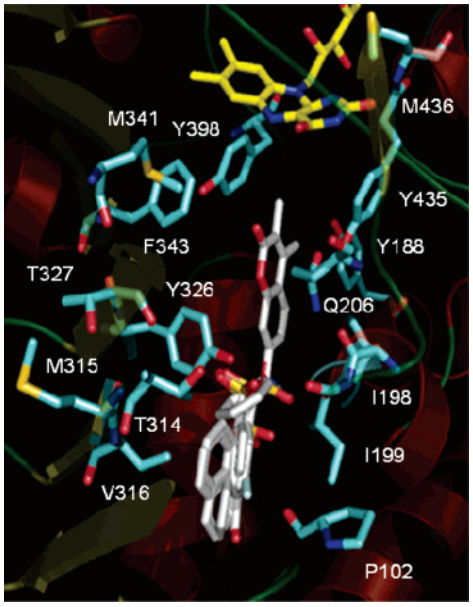

Figure 2. Incorporation of the molecular alignment used in CoMFA analysis into the rMAO-B binding site.

3D-QSAR Studies. Although most of the observations reported above surely helped to clarify some important aspects of the SAFIRs and SSRs, an exact picture of the main interactions taking place at the active sites of the two rat isoenzymes was still missing. To overcome this limitation, a combined modeling study was carried out through CoMFA,[24] homology building, and docking simulations. The purpose of this study was twofold: (i) to gain further insights on the physicochemical nature and precise spatial location of the key interactions of the 7-substituents responsible for the observed enzyme affinities and, more importantly, selectivities and (ii) to confirm, complement, and better interpret the results of previous studies conducted by some of us on different sets of coumarin derivatives.[19,20]

Besides classical CoMFA of MAO-A and MAO-B affinities, expressed as pIC_{50}, an additional 3D-QSAR analysis was executed to model directly B/A selectivity, measured as the difference between pIC_{50} of MAO-B and pIC_{50} of MAO-A (ΔpIC_{50}). Molecular alignment, the most critical step in CoMFA, was made by adopting the same criteria reported in our previous work[19] and taking advantage of the knowledge of the space accessible to 7-substituents to the binding site of MAO-B (see Figure 2).

Along with classical CoMFA interaction fields (i.e., steric and electrostatic fields) computed within SYBYL,[25] the lipophilic field, calculated by the CLIP program,[26] was also used as an additional descriptor to better explain the variance in the biological data. The results of the PLS analyses, obtained by

Table 2. Statistics of the CoMFA-GOLPE Models of MAO-B Inhibition ($n = 38$)

model	field type	q^2 [a]	ONC[b]	r^2 [c]	SDEP[d]
I	Ste (S-B)	0.692	3[e]	0.821	0.756
II	Ele (E-B)	0.805	2	0.885	0.601
III	Lipo (L-B)	0.674	2	0.785	0.776
IV	Ele + Ste (ES-B)	0.830	2	0.899	0.561
V	Lipo + Ste (LS-B)	0.677	2	0.787	0.773
VI	Ele + Lipo (EL-B)	0.834	2	0.895	0.554
VII	Ste + Ele + Lipo (SEL-B)	0.837	2	0.906	0.549

[a] Leave-one-out squared cross-validated correlation coefficient. [b] Optimal number of PLS components. [c] Squared correlation coefficient. [d] Standard deviation of error of predictions. [e] Two-component statistics of model I: $q^2 = 0.615$; $r^2 = 0.735$; SDEP = 0.844.

Table 3. Statistics of the CoMFA-GOLPE Models of MAO-A Inhibition ($n = 38$)

model	field type	q^2 [a]	ONC[b]	r^2 [c]	SDEP[d]
VIII	Ste (S-A)	0.727	2	0.819	0.461
IX	Ele (E-A)	0.673	2	0.811	0.505
X	Lipo (L-A)	0.708	2	0.802	0.447
XI	Ele + Ste (ES-A)	0.751	2	0.859	0.441
XII	Lipo + Ste (LS-A)	0.738	2	0.823	0.452
XIII	Ele + Lipo (EL-A)	0.659	2	0.819	0.515
XIV	Ste + Ele + Lipo (SEL-A)	0.789	2	0.881	0.406

[a] Leave-one-out squared cross-validated correlation coefficient. [b] Optimal number of PLS components. [c] Squared correlation coefficient. [d] Standard deviation of error of predictions.

means of the leave-one-out cross-validation procedure[27] and GOLPE[28] (for data pretreatment and analysis), are listed in Tables 2, 3, and 4 for MAO-B affinity, MAO-A affinity, and B/A selectivity, respectively.

Some differences from our previous CoMFA study on coumarins[19] were observed in the modeling of MAO-B and MAO-A inhibition leading to PLS models I−VII and VIII−XIV listed in Tables 2 and 3, respectively. Both MAO-B and MAO-A affinities seem to be modulated by steric, lipophilic, and electrostatic effects rather than by the electrostatic and lipophilic ones, respectively, as found in our previous analysis.[19] This apparent contradiction can be ascribed to the different data sets used in the two 3D-QSAR studies. Indeed, while in our previous CoMFA study most of the structural variations have been made on the 7-benzyloxy group, in the current set of inhibitors, more systematic variations in the 7-bridge were investigated, and therefore, the new PLS models could be considered complementary rather than alternative to previous models.

Isocontour maps from the three-field PLS models VII (MAO-B) and XIV (MAO-A) were developed to facilitate the spatial location of the main interactions influencing the inhibitory potency. The following color code was used to point out steric, electrostatic, and lipophilic interactions: red/green to indicate regions for unfavorable/favorable steric effects, gray/magenta to indicate contour zones where a high electron density is unfavorable/favorable to affinity, and cyan/yellow to display zones where unfavorable/favorable lipophilic interactions may occur. As can be seen in Table 1, the introduction of a halogen atom in the meta position of the 7-benzyloxy group significantly increased the binding affinities. Indeed, this observation is in full agreement with the appearance of favorable signals in the meta region in steric, electrostatic, and lipophilic isocontour maps, indicated in Figure 3 by green, magenta and yellow areas, respectively. Similarly, the negative effects on MAO-B inhibitory activity exerted by the sulfonate group of derivatives **23**−**26** were pointed out clearly in the three isocontour maps of Figures 4. The poor MAO-B affinity of the phenoxy derivative **29** gave rise to unfavorable signals again in the three different isocontour maps. Other significant signals came from specific isocontour maps. The increased MAO-B affinity of monomethyl and dimethyl derivatives in positions 3 and 4 was well explained by a green zone in the steric map of Figure 3a, whereas the high MAO-A affinity of *p*-nitrophenyl sulfonate **25** was accounted for by magenta polyhedra in the electrostatic contour map (Figure 4b). Sterically forbidden areas were impacted by phenyl rings of the long inhibitors **33**, **34**, **37**, and **38**, which were endowed with poor MAO-A affinity. The steric maps of MAO-A (Figure 4a) furnished readily interpretable negative red signals for the sulfoxide derivative **22**, but surprisingly, no green area for the OSO_2 groups of the highly active sulfonic esters **23**−**26** was detected. Interestingly the different MAO-B affinities of chiral alcohols **31** can be explained, at least in part, by the electrostatic and lipophilic isocontour maps. Accordingly the distomer (−)-**31** and eutomer (+)-**31** should have the *R* and *S* absolute configurations, respectively.

Given that the main purpose of our research was the detection of the molecular determinants of B/A selectivity, particular

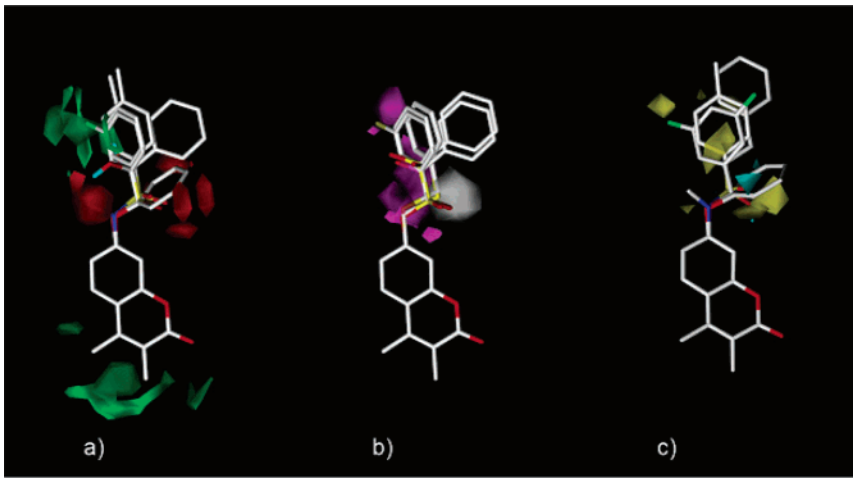

Figure 3. CoMFA-GOLPE (MAO-B affinity) (a) steric, (b) electrostatic, and (c) lipophilic isocontour maps. (a) Contour levels are −0.0006 (red) and 0.00035 (green). Inhibitors **9** ($pIC_{50} = 8.36$), (+)-**31** ($pIC_{50} = 7.55$), (−)-**31** ($pIC_{50} = 6.52$), **29** ($pIC_{50} = 5.49$), **27** ($pIC_{50} = 4.50$), and **24** ($pIC_{50} = 4.50$) are shown to help interpretation. (b) Contour levels are 0.0018 (gray) and −0.00075 (magenta). Inhibitors **39** ($pIC_{50} = 8.55$), **30** ($pIC_{50} = 7.74$), **21** ($pIC_{50} = 7.40$), **36** ($pIC_{50} = 6.06$), **12** ($pIC_{50} = 5.89$), and **15** ($pIC_{50} = 4.26$) are shown to help interpretation. (c) Contour levels are 0.0011 (yellow) and −0.0008 (cyan). Inhibitors **9** ($pIC_{50} = 8.36$), **34** ($pIC_{50} = 7.28$), **28** ($pIC_{50} = 6.49$), **42** ($pIC_{50} = 8.52$), **29** ($pIC_{50} = 5.49$), and **27** ($pIC_{50} = 4.50$) are shown to help interpretation.

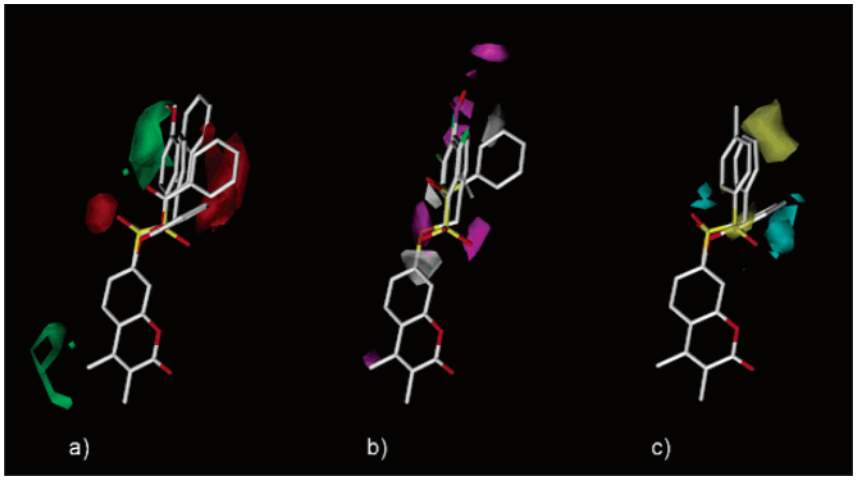

Figure 4. CoMFA-GOLPE (MAO-A affinity) (a) steric, (b) electrostatic, and (c) lipophilic isocontour maps. (a) Contour levels are −0.00055 (red) and 0.0009 (green). MAO-A inhibitors **24** (pIC_{50} = 7.33), **26** (pIC_{50} = 7.15), **16** (pIC_{50} = 5.02), **22** (pIC_{50} = 4.73), **29** (pIC_{50} = 4.50), and **38** (pIC_{50} = 4.00) are shown to help interpretation. (b) Contour levels are 0.00099 (gray) and −0.00073 (magenta). Inhibitors **25** (pIC_{50} = 7.90), **41** (pIC_{50} = 6.91), **42** (pIC_{50} = 6.17), **36** (pIC_{50} = 5.55), and **21** (pIC_{50} = 5.00) are shown to help interpretation. (c) Contour levels are −0.0037 (yellow) and 0.0001 (cyan). Inhibitors **24** (pIC_{50} = 7.33), **26** (pIC_{50} = 7.15), **22** (pIC_{50} = 4.73), and **29** (pIC_{50} = 4.50) are shown to help interpretation.

Table 4. Statistics of the CoMFA-GOLPE Models of B/A Selectivity (n = 38)

model	field type	q^2 [a]	ONC[b]	r^2 [c]	SDEP[d]
XV	Ste (S-B/A)	0.751	3[e]	0.867	0.840
XVI	Ele (E-B/A)	0.897	2	0.941	0.539
XVII	Lipo (L-B/A)	0.829	2	0.881	0.696
XVIII	Ele + Ste (ES-B/A)	0.883	2	0.932	0.575
XIX	Lipo + Ste (LS-B/A)	0.832	2	0.834	0.690
XX	Ele + Lipo (EL-B/A)	0.908	2	0.944	0.510
XXI	Ste + Ele + Lipo (SEL-B/A)	0.889	2	0.926	0.560

[a] Leave-one-out squared cross-validated correlation coefficient. [b] Optimal number of PLS components. [c] Squared correlation coefficient. [d] Standard deviation of error of predictions. [e] Two-component statistics of model XV: q^2 = 0.665; r^2 = 0.797; SDEP = 0.974.

attention was devoted to the analysis of selectivity data. A closer look at the square plot shown in Figure 1 provided a clear view of the selectivity associated with each compound and allowed easy detection of the most potent and highly selective MAO-A and MAO-B inhibitors. However, additional and more important insights on SSRs were gained from a CoMFA study of selectivity data, expressed as ΔpIC_{50}. The statistics of the CoMFA-GOLPE models reported in Table 4 indicated that B/A selectivity was governed mainly by electrostatic effects, whereas lipophilic and, to a major extent, steric effects played a less important role. The one-field electrostatic model XVI presented the best statistics. Its very good fitting power (r^2 = 0.941) can be easily appreciated from a plot of calculated versus experimental ΔpIC_{50} selectivity values reported in Figure 5.

Isocontour maps, calculated from model XVI and displayed in Figure 6, helped to interpret and locate at the 3D level the electrostatic interactions modulating B/A selectivity. The absence of signals close to position 3 and/or position 4 of the coumarin ring seemed to indicate that methyl groups in those regions did not play a relevant role in modulating B/A selectivity. This result apparently contrasted with the significantly higher B/A selectivity observed for 7-benzyloxy-3-methylcoumarin (**8**) compared with 7-benzyloxy-4-methyl (**7**), 7-benzyloxy-3,4-dimethyl (**9**), and the 7-benzyloxy-3,4-unsubstituted (**6**) derivatives. The lack of a definite signal in position 3 may be due to the fact that there was only one 3-methyl derivative in the data set and that only very strong signals, coming from substantial changes in ΔpIC_{50} selectivity values, were selected and represented in the isocontour maps. The close

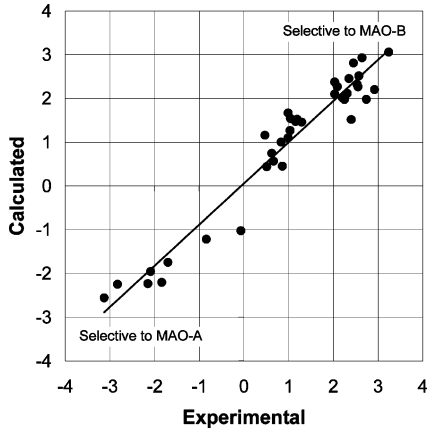

Figure 5. Scatter plot of the experimental vs calculated B/A selectivity values (ΔpIC_{50}) (from model XVI, Table 4). The bisector represents the case of perfect correlation (r^2 = 1).

Figure 6. CoMFA-GOLPE (B/A selectivity) electrostatic isocontour maps. Contour levels are 0.002 (gray) and −0.00083 (magenta). MAO-B selective inhibitors **38** (ΔpIC_{50} = 3.24), **34** (ΔpIC_{50} = 2.64), **42** (ΔpIC_{50} = 2.35), **41** (ΔpIC_{50} = 2.03), **11** (ΔpIC_{50} = 1.29), and **29** (ΔpIC_{50} = 0.99) are shown along with the MAO-A selective inhibitor **23** (ΔpIC_{50} = −1.84) to help interpretation.

inspection of Figure 6 allowed a straightforward interpretation of the influence of substituent electronic properties on selectivity. The different electron density localized on the α and β positions of the bridge connecting the coumarin ring to the phenyl ring seemed to be responsible for the observed B/A selectivity. Indeed, strongly electronegative atoms (i.e., oxygen and sulfur) in the α position may favorably contact the magenta region and therefore improve B/A selectivity (i.e., **8**). Close contacts in the same zone may also furnish a sound explanation for the significant fall of B/A selectivity caused by the inversion of

Table 5. Active Site Residues of Both Human MAO Isoenzymes with Divergent Residues in Italic Font and with Differing Residues in Rat in Parentheses

hMAO-B	hMAO-A	hMAO-B	hMAO-A
P102	*A111*	*Y326*	*I335*
Y188	Y197	T327	T336
I198	I207	M341	M350
I199	*F208*	F343	F352
Q206	Q215	Y398	Y407
T314	*C323*	Y435	Y444
M315	M324	M436	M445
I316 (V316)	I325		

the oxymethylene bridge (**6** vs **10**; $\Delta pIC_{50} = 2.09$ vs 0.66). Electronegative moieties in the gray region near the β position accounted for the inverted, or strongly decreased, B/A selectivity observed for highly MAO-A selective sulfonates **23**−**26** and phenoxy derivative **29**. Magenta regions on the left-hand side of Figure 6 can be reached by phenyl rings of the long MAO-B selective inhibitors **32**−**34** and **37**−**38** and by the halogen atoms of inhibitors **39**−**42**. The high B/A selectivity of cinnamyl derivatives **37** and **38** may also be due to the increased electron density of their alkenyl double bonds placed on the γ position (magenta region) of the bridge connecting coumarin to the phenyl ring.

Docking Studies. To help interpretation of SAFIRs and to increase our understanding of the main binding interactions at the MAO active sites, a docking study was performed on some selective inhibitors. Since inhibition data referred to MAOs from rat brain mitochondria, we first developed a 3D homology model of rMAO-B, for which no X-ray crystallographic data are available. Fortunately, this was not such a difficult task because rat and human enzymes presented highly similar amino acid sequences (88.6% sequence identity; 519 and 520 amino acids for rat and human enzyme, respectively) and almost identical amino acid residues in the binding sites where the only difference resulted from the substitution of I316 (human) with V316 (rat). A number of active site residues of the two human MAO isoenzymes are reported in Table 5 to help the reader to identify the exact correspondence with the rat isoforms and to safely compare human and rat X-ray and docking models.

The 3D model of rMAO-B was constructed through comparative protein structure modeling within the Modeller 8.1 program[29] after sequence alignment performed with Clustal_X[30] (see Experimental Section).

Our docking investigation focused on inhibitor **9**, which showed the highest MAO-B affinity ($pIC_{50} = 8.36$) along with a remarkable B/A selectivity ($\Delta pIC_{50} = 2.20$). The GOLD 2.2 program was used to carry out docking simulations,[31] since in several studies it yielded better performances compared to other similar programs.[32−35] It must be noted that a recent exhaustive study of a large number of enzyme−inhibitor complexes,[35] whose X-ray crystallographic structures were retrieved from the PDB, showed that for the most applied docking programs, including GOLD, a limited correspondence between experimental and docking poses and, moreover, the various scoring functions used in the tested programs were not able to calculate and rank correctly the binding energies of many experimental complexes. The lesson to be learned from such a study is that results of docking simulations have to be taken into account with much caution because different binding modes may result even from structurally close ligands and, furthermore, the same ligand may experience multiple binding poses within a relatively close energy window.

Keeping in mind the above limitations, we conducted the docking simulations with GOLD 2.2. An analysis of principles and methods adopted by GOLD for energy calculations, conformational search and clustering, and energy ranking is briefly presented in the Experimental Section, whereas a fully detailed description may be found elsewhere.[36] An in-depth look at the conformer population of inhibitor **9** generated during the docking simulations into the rMAO-B active site revealed that a convergent binding mode was largely adopted. In the majority of the docking poses the coumarin ring was located in front of the FAD moiety with the coumarin carbonyl facing Y435 (data not shown). A hierarchical cluster analysis, carried out on the best bound conformers generated during the docking runs, revealed that all the molecules could be collected in one prevalent geometric group within an rms value of 1.96Å and a fitness score[37] of 52.28 kJ/mol for the best scored (most stable) complex. Additional docking studies were subsequently carried out to more deeply analyze key regions of the binding pocket, in particular those near the FAD cofactor, to find other energetically viable binding modes. For this purpose, the coumarin ring of the best bound conformer was turned 180° around and a number of physical constraints (see Experimental Section) were adopted before starting the second series of docking runs. The resulting docking poses, showing a differently oriented coumarin ring but similarly bound 7-benzyloxy group, maintained high fitness scores (in the range 46.6−49.9 kJ/mol). The small energy differences among the fitness scores from constrained and unconstrained docking (<5 kJ/mol) suggested that the binding interactions were most likely driven by the benzyloxy group, which acted as the molecular anchor of the inhibitor, whereas the coumarin ring might assume two different binding topologies (data not shown). Surprisingly, among the best scored docking poses, GOLD finds no hydrogen bond (HB) between the oxygen atom of the benzyloxy group and an eventual HB donating group in the enzymatic cleft. This result was unexpected because the formation of a HB might have explained the selective inhibition of MAO-B by 7-benzyloxycoumarin derivatives and the decrease of affinity observed when the benzyloxy oxygen atom was substituted by unsaturated and saturated carbon and sulfur atoms (compare the affinities of **9** vs **17**, **18**, and **21**). A careful visual analysis of the docking pose of **9** revealed that its ether oxygen was indeed relatively close to the phenolic group of Y326 and, therefore, potentially able to form a HB. This observation prompted us to run further docking simulations by increasing the sensitivity of GOLD to detect such a HB (see Experimental Section). Under these experimental conditions, HB was indeed found in several viable docking poses featuring an energetically acceptable fitness score (nearly 47−48 kJ/mol), irrespective of the orientation of the coumarin ring. The high MAO-B affinity and B/A selectivity of 7-benzyloxycoumarins might therefore be plausibly accounted for by the formation of this HB. Nevertheless, the formation of an alternative network of HBs linking benzyloxy oxygen to suitably positioned HB donating residues of the enzyme (i.e., T201, I199, and Q206) through a bridge consisting of a structural water molecule could not be ruled out. For this reason and with the aim to verify whether even additional water molecules might play a role in ligand binding to rMAO-B, a molecular mapping of the enzyme binding site was undertaken. A reasonable detection and 3D location of structural water molecules in proteins can be efficiently performed by means of the software GRID[38] (see Experimental Section), which calculates the most favorable interaction energies of a selected chemical probe positioned at each node of a properly sized grid surrounding the protein. The binding site of rMAO-B was subjected to GRID, and an arbitrary cutoff value of −9 kcal/mol was chosen to

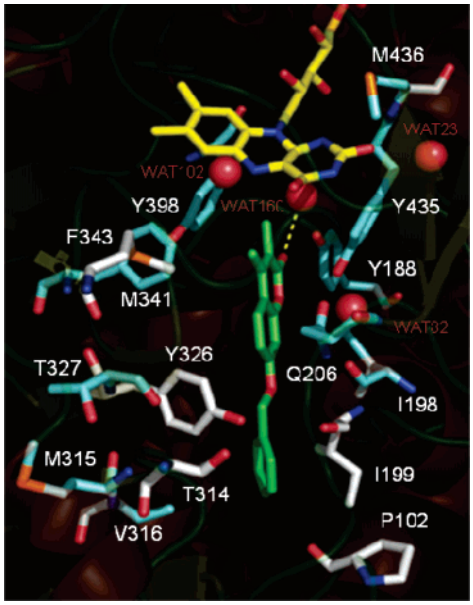

Figure 7. Docking pose of inhibitor **9** into rMAO-B binding site. Amino acid residues and FAD cofactor are represented in stick form, colored according to the atom code (C atoms in cyan and yellow for amino acid residues and cofactor, respectively); structural water molecules are represented as red balls. Differing residues with MAO-A, which are P102/A111, I199/F208, T314/C323, and Y326/I335, are highlighted as white sticks. Yellow dashed lines are drawn among electronegative atoms likely involved in HB interactions.

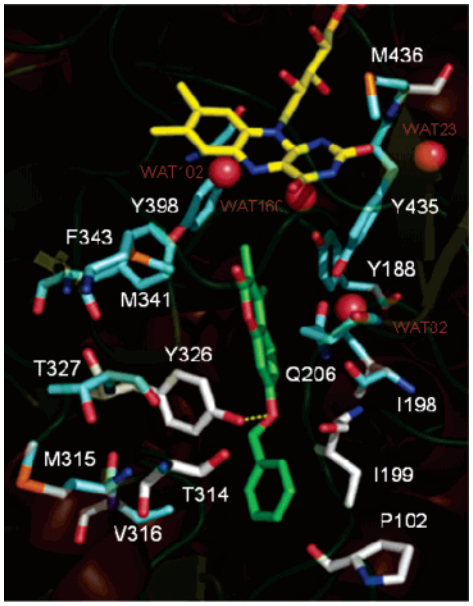

Figure 8. Alternative docking pose of inhibitor **9** into rMAO-B showing a HB between the oxygen atom of the ether bridge and Y326 (see text). Color codes are as in Figure 7.

detect the most favorable hot spots for a water molecule used as chemical probe. Four water molecules, labeled as WAT23, WAT82, WAT102, and WAT160 according to the numbering reported in the hMAO-B crystallographic structure[10] (coded as 1OJC in PDB), were intercepted in proximity of the FAD cofactor. Two of them, WAT102 and WAT23, have already been detected in the crystallographic analysis of hMAO-B,[10] while a third, WAT160, was found below the FAD pyrimidine ring, embedded in the π-system of the aromatic side chains of Y398 and Y435.[39] The fourth water molecule, WAT82, was located about 3.70 Å apart from the α carbons of I198 and G205. A docking simulation of inhibitor **9** into the rMAO-B binding site containing the four water molecules generated two most energetically favored geometric clusters, consisting of four and six conformers, corresponding to two basic docking poses that differed mainly in the topology of the coumarin ring. In the docking pose represented in Figure 7, the coumarin ring adopted the same topology, found previously in the unconstrained docking, with the carbonyl oxygen of coumarin engaged in a HB with WAT160. From an energetic point of view, only a negligible variation of the fitness score (52.04 vs 52.28 kJ/mol) resulted from the docking run with and without water molecules. In the second alternative and isoenergetic binding mode (52.03 kJ/mol), the coumarin ring was turned 180°, as found previously in the constrained docking simulation. Again, it must be stressed that the expected HB between the benzyloxy oxygen and a relatively close HB donating residue, notably Y326, was not detected by GOLD among the top-ranking solutions. Therefore, an additional investigation was conducted with GRID by first sampling with the water probe the docked complexes developed by including the four water molecules. The most favorable interactions were located in proximity of the FAD cofactor, and for much lower cutoff values only (−5.5 vs −9.0 kcal/mol), the regions surrounding the ether bridge of **9** were sparsely intercepted (data not shown).

Finally, a further docking run was carried out, again tuning GOLD to check for a HB between the oxygen of the ether bridge of **9** and the hydroxyl group of Y326, analogous to what was previously done on the docking runs without water molecules. Again, the most favorable docking poses showed the expected HB at the expense of a limited loss of fitness score (nearly 5 kJ/mol). In this binding mode, the coumarin ring, as shown Figure 8, lost the HB with WAT160 and was oriented differently compared to that shown in Figure 7.

Interestingly, all the proposed binding modes of **9** are in full agreement with the increased MAO-B affinity observed for *m*-halogenophenyl derivatives whose halogens interacted with a hydrophobic region delimited by I164, L167, F103, and W119.

In summary, our extensive docking simulations, conducted with and without potential structural water molecules, suggested the formation of a key HB between the benzyloxy oxygen and the phenolic group of Y326, and this provided a significant clue for the interpretation of the MAO-B selective inhibition and MAO-B affinity modulation observed in 7-substituted coumarins.

An additional docking study was performed on the highly potent and selective MAO-A inhibitor **25** by applying the same methodology described for MAO-B selective inhibitor **9**. Given that water molecules had been deleted from the crystal structure of rMAO-A,[11] GRID mapping with water as a probe was not performed because we judged the identification of reliable hot spots for truly structural water molecules too risky and arbitrary.

Phenyl sulfonate **25** was docked into the binding site of rMAO-A whose 3D structure was retrieved from the PDB (coded as 1O5W). No significant insights about high MAO-A affinity and B/A selectivity of phenyl sulfonate inhibitors were gained from such a docking simulation. These disappointing results prompted us to apply alternative modeling approaches. Keeping in mind that GOLD explores a full conformational flexibility for the ligand but not for the proteins, we first undertook a molecular dynamics (MD) study on both MAOs to detect eventual differences in the conformational mobility of the amino acids in the two binding sites. Preliminary MD data[40] indeed suggested a much higher conformational flexibility of Q215 in MAO-A than the corresponding Q206 in MAO-B.

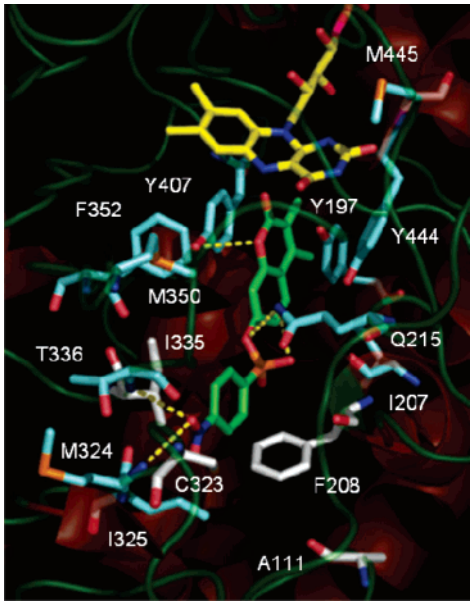

Figure 9. Docking pose of inhibitor **25** into rMAO-A active site. Color codes are as in Figure 7. The binding conformation on display showed the coumarin ring facing the FAD isoalloxazine ring.

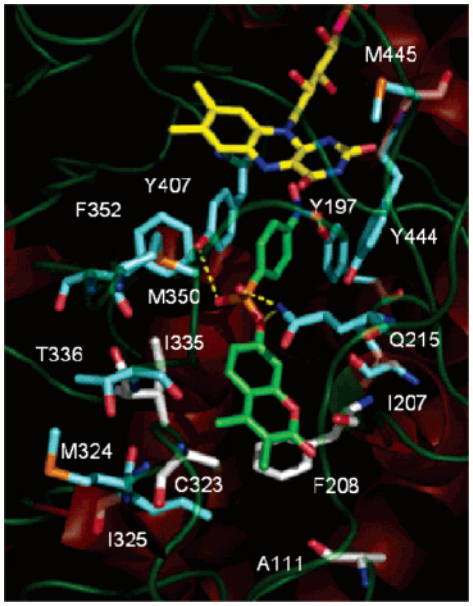

Figure 10. Alternative docking pose of inhibitor **25** into rMAO-A active site. Color codes are as in Figure 7. The binding conformation on display showed the coumarin ring close to the cavity entrance.

Therefore, docking simulations on rMAO-A were repeated starting from a number of energetically viable conformations of the Q215 side chain. Results from GOLD runs suggested multiple docking poses characterized by quite diverse binding modes but comparable fitness scores. Analysis of top-ranking docking solutions indicated two opposite binding modes as found for rMAO-B: one with the coumarin and the other with the *p*-nitrophenyl ring facing the FAD isoalloxazine ring system. The two binding poses most consistent with our SAFIR and SSR models are reported in Figures 9 and 10. They featured comparable fitness scores and a similar extended conformation of the Q215 side chain. An in-depth analysis of the pivotal interactions stabilizing the enzyme−inhibitor complex reported in Figure 9 suggested that the higher MAO-A affinity and selectivity of phenyl sulfonates might be ascribed to the likely formation of a network of strong HBs linking the oxygen atoms of the sulfonate moiety to hydrogen atom(s) of the NH_2 group of the Q215 side chain. This hypothesis, supported by our MD simulations (data not shown), was based on the assumption that an optimal HB distance exists between the proximal oxygen atom of SO_2 of inhibitor **25** and the NH_2 group of Q215, which was also engaged in a HB with the oxygen atom of the sulfonate group attached directly to the coumarin ring. In addition, GOLD detected further HBs established by the nitro group of the *p*-nitrophenyl moiety of **25** with T336 and M324 and by the lactonic oxygen of the coumarin ring with the phenolic group of Y407. Notably, a closer view of the docked complex revealed that **25** might interact also with C323, whose SH group seemed to be placed at a proper distance to make a HB with an oxygen atom of the nitro group. This may provide an additional explanation for the increased MAO-A affinity and B/A selectivity shown by **25** compared to **23**. As a matter of fact, this HB was not detected by GOLD. Interestingly, in a slightly different binding conformation, GOLD indeed detected a close contact (van der Waals-like interaction) between C323 and the phenyl ring of **25**. Such an interaction has also been described by Mattevi for the binding of clorgyline to h-MAO-A.[12] Since C323 is one of the few amino acids that differentiate rMAO-A from rMAO-B, its interaction with inhibitors, irrespective of its nature, might in principle provide MAO-A selectivity to some classes of MAOIs. However, its potential role in the binding of MAO-A-selective phenyl sulfonate inhibitors deserves further investigation.

In an alternative binding mode of **25** (Figure 10), a different network of HBs may be seen. It involves the formation of a number of HBs among the sulfonate group, the two hydrogen atoms of the NH_2 group of Q215, and the phenolic group of Y407. Moreover, GOLD showed that the nitro group was again engaged in a HB but with Y197. It is worth noting that in both docked complexes reported in Figures 9 and 10 two different oxygen atoms of the sulfonate group seem to be involved in the formation of HBs: one from the sulfonyl group and the other from the coumaryloxy moiety (SO_2*O*-coum), in agreement with the higher MAO-A affinity observed for sulfonates **23**−**26** compared with other sulfonyl-containing derivatives such as **14** and **36**. Both docking models also explained the significant enhancement of affinity and MAO-A selectivity determined by the introduction of the nitro group in the para position of the phenyl ring of inhibitor **23**. Two plausible and favorable interactions could take place: (i) the formation of HBs with HB donating groups in the enzyme; (ii) a $\pi-\pi$ stacking interaction with F208 or FAD. Our docking models also allowed us to also interpret the low MAO-A affinity observed for the long alkoxy (i.e., **33** and **34**) and cinnamyl (i.e., **37** and **38**) derivatives, which with their phenyl rings might impact a zone occupied by I325 and L337, and for inhibitor **29** whose phenoxy ring could collide with the side chain of I335.

Comparison among CoMFA and Docking Models. The overlay of the CoMFA isocontour maps on the corresponding MAO-A and MAO-B active sites, limited to the steric maps for easier interpretation, lent further support to the hypothesized docking models. Figure 11 showed the steric maps, already reported in Figure 4a, embedded into the MAO-B binding site. Both the binding modes reported in Figures 7 and 8 might be compatible with the imported CoMFA steric maps. However, for the sake of simplicity, only that derived from Figure 8 was displayed in Figure 11 (without water molecules). Amino acid residues likely involved in steric clashes with low active inhibitors (i.e., **29** and phenyl sulfonates **23**−**26**) were indicated in red, whereas in green were represented apolar side chains of

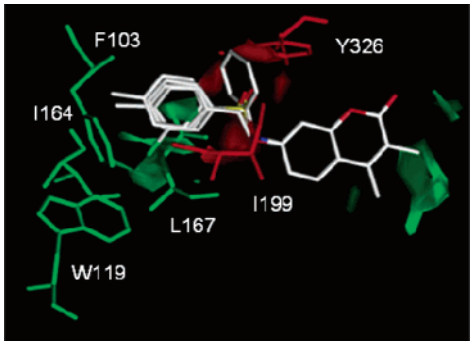

Figure 11. Active binding site of rMAO-B showing the steric CoMFA isocontour maps imported from Figure 3a. Inhibitors **40** ($pIC_{50} = 8.48$), **9** ($pIC_{50} = 8.36$), **29** ($pIC_{50} = 5.49$), **24** ($pIC_{50} = 4.50$), and **27** ($pIC_{50} = 4.50$) are shown to help interpretation.

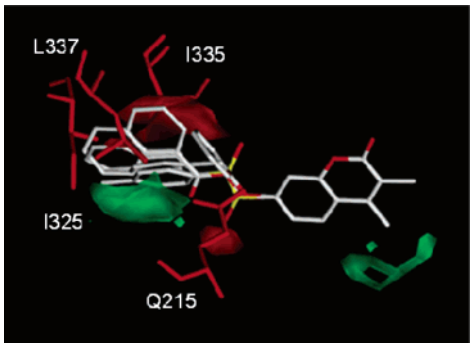

Figure 12. Active binding site of rMAO-A showing the steric CoMFA isocontour maps imported from Figure 4a. MAO-A inhibitors **24** ($pIC_{50} = 7.33$), **16** ($pIC_{50} = 5.02$), **22** ($pIC_{50} = 4.73$), **34** ($pIC_{50} = 4.64$), **29** ($pIC_{50} = 4.50$), and **38** ($pIC_{50} = 4.00$) are shown to help interpretation.

Chart 3. Chemical Structure of the Most B/A Selective Inhibitor

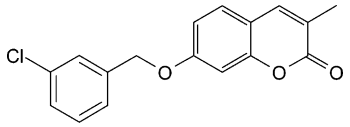

43

F103, I164, W119, and L167, which constituted the lipophilic region surrounding the meta and, to a lesser extent, para halogen atoms of highly active inhibitors (i.e., **39**−**42**). Figure 12 referred to the steric map, already shown in Figure 4a, embedded in the MAO-A binding site. Between the two binding topologies suggested by docking studies, the one reported in Figure 9 seemed more compatible with the observed CoMFA steric maps. Again, in red were highlighted the amino acid residues generating steric hindrance to low active MAO-A inhibitors such as **16**, **22**, **29**, **34**, and **38**, whose aromatic rings might collide with side chains of I325, I335, and L337. The low active MAO-A inhibitor **22** might also affect the Q215 side chain with its sulfonyl group.

Rational Design of a New Potent and MAO-B Selective Inhibitor. To challenge the external predictive ability of our models and to prepare an inhibitor with high MAO-B affinity and improved B/A selectivity, we designed a novel coumarin derivative on the basis of our CoMFA and docking models developed herein and on a QSAR model derived some years ago for meta-substituted benzyloxycoumarins.[19] 7-(*m*-Chlorobenzyloxy)-3-methylcoumarin (**43**, Chart 3), whose structure is reported below, emerged as a simple and potentially strong and selective MAO-B inhibitor.

Docking simulations of compound **43** into the active site of rMAO-B showed almost identical binding modes and similar fitness values compared to lead derivative **9**. The fitness values for the docking poses of compound **43** in rMAO-A indicated less stable enzyme complexes, likely suggesting a higher selectivity of the newly designed inhibitor **43** compared to inhibitor **9**. In line with our expectations, the evaluation of the inhibitory affinity of compound **43** resulted in a very high MAO-B affinity ($pIC_{50} = 8.29$), a very low MAO-A affinity ($pIC_{50} = 4.90$), and as a consequence an outstanding B/A selectivity ($\Delta pIC_{50} = 3.39$). This selectivity value, even better than predicted, was the highest within the entire series of inhibitors examined herein.

Conclusion and Prospects

In this investigation we reported 3D-QSAR and docking studies of a new series of substituted coumarin inhibitors designed to explore in a systematic manner the substituent effects at position 7. On the basis of previous[19,20] and herein reported results, the major structural determinants of rMAO affinity and B/A selectivity were established for this biologically important and easily accessible class of natural compounds.[41] We demonstrated that rMAO affinity and selectivity can be efficiently modulated by appropriate modifications of length, size, and chemical nature of the substituents at position 7 and by introducing methyl groups in positions 3 and 4. Our findings pointed out a crucial, undisclosed role of the methyl group in position 3 to obtain highly potent and selective MAO-B inhibitors. This hypothesis was experimentally confirmed with the design and biological evaluation of a new 3-methyl-substituted coumarin (compound **43**), which proved to be a highly potent and the most selective MAO-B inhibitor within the entire series examined in this work. The systematic structural variation of the sulfur-containing linker at position 7 revealed the pivotal role of the sulfonate group, directly linked to the coumarin ring, for high MAO-A affinity and selectivity.

CoMFA-GOLPE studies enabled the identification of the physicochemical nature and spatial location of the main binding interactions modulating the enzymatic affinity and selectivity. Convergent results from CoMFA models and docking simulations indicated that MAO affinities depended on electronic, steric, and lipophilic characteristics of the 7-substituted coumarins and confirmed that the benzyloxy and sulfonate groups presented the best structural profiles for optimal interactions with MAO-B and MAO-A binding sites. Indeed, the docking poses resulting from GOLD disclosed favorable interactions of the benzyloxy group, which took place in a smaller cavity of the MAO-B binding site, relatively far from the FAD cofactor, whereas the coumarin ring binds in the major lipophilic cage delimited by FAD, Y326, Y398, and Y435 of rMAO-B, assuming two possible different conformations. Appropriate docking simulations suggested that the ether oxygen of the benzyloxy moiety may form a HB with the phenolic group of Y326, and this may account for both the high MAO-B affinity and B/A selectivity of 7-benzyloxycoumarins. The same interaction cannot take place in the rMAO-A binding site, which presents an isoleucine (I335) in place of a tyrosine (Y326).

As far as the MAO-A selectivity is concerned, the docking model of the highly selective MAO-A inhibitor **25** in Figure 9 suggested that the higher affinity of the phenyl sulfonate inhibitors for MAO-A might result from the formation of a network of HBs linking the oxygen atoms of the sulfonate moiety to the HB donating side chain of Q215 and the oxygen atom within the coumarin ring to phenolic group of Y407.

Further HBs and/or a $\pi-\pi$ stacking interaction with F208 could be established by the *p*-nitrophenyl moiety of **25**. An alternative binding mode based on an opposite ligand binding topology and a different HB network (Figure 10) cannot be ruled out. It would be interesting to cocrystallize inhibitor **25** with rMAO-A to lend support to our binding hypotheses.

In conclusion, the present study confirmed and reinforced the validity of the interaction models proposed by our group on MAO-B inhibitors[19,20] and deepened our understanding of the structural requirements for high MAO affinity and selectivity. The easy synthetic accessibility and potentially low toxicity of coumarins make them "privileged scaffolds" for preparing new inhibitors with improved in vitro affinity. However, it could be expected that the extreme lipophilic nature of 7-benzyloxy-3,4-substituted coumarin derivatives might reduce their in vivo potency as a result of a limited water solubility and poor bioavailability. Interestingly, the discovery of high MAO-B affinity and selectivity of 3-methylcoumarins might in part alleviate this problem, since the overall molecular lipophilicity (log *P*) is lowered at least by 0.5 log unit compared with the corresponding 3,4-dimethyl congeners. Finally, to obtain inhibitors with definitely improved pharmacokinetic properties, new and original classes of MAO-A and MAO-B selective inhibitors have been designed and are currently being developed in our laboratories.

Experimental Section

Chemistry. Starting materials, reagents, and analytical grade solvents were purchased from Sigma-Aldrich, Inc. Chromatographic separations were performed on silica gel (15−40 mesh, Merck) by flash methodology. Melting points (mp) were determined by the capillary method on a Stuart Scientific SMP3 electrothermal apparatus and are uncorrected. Elemental analyses were performed on a Euroea 3000 analyzer for C, H, and N; the results agreed to within ±0.40% of the theoretical values. IR spectra were recorded using potassium bromide disks on a Perkin-Elmer FT-IR spectrophotometer; only the most significant IR absorption bands are reported. ^{1}H NMR spectra were recorded in $CDCl_3$ (unless otherwise specified) at 300 MHz on a Varian Mercury 300 instrument. Chemical shifts are expressed in δ (ppm) and coupling constants *J* in hertz (Hz). The following abbreviations were used: s (singlet), d (doublet), t (triplet), dd (double doublet), dt (double triplet), m (multiplet). Signals due to OH protons were located by deuterium exchange with D_2O.

The syntheses of compounds **6**, **7**, **9**−**11**, **18**−**20**, **23**−**26**, **28**, **32**, and **39**−**42** have been described in ref 19. Compounds **12**−**14** and **30** have been reported in ref 20. Compounds **34**,[42] **35**,[43] and **38**[44] were synthesized according to published procedures with slight modifications; their analytical and spectral data were in agreement with those reported in the literature.

Synthesis of 3-Methylcoumarin Derivatives 8 and 43. Starting 7-hydroxy-3-methylcoumarin **5** was prepared via a classical Perkin condensation from 2,4-dihydroxybenzaldehyde and propionic anhydride according to Gia et al.[45] An amount of 1.0 mmol of **5** (176 mg) was refluxed with 2.0 mmol of either benzyl bromide or 3-chlorobenzyl bromide and anhydrous potassium carbonate (1.0 mmol, 138 mg) in 10 mL of absolute ethanol for 2 h. The warm solution was filtered and cooled to room temperature to give a pure crystalline solid.

7-Benzyloxy-3-methyl-2*H*-chromen-2-one (8). 60% yield; mp 129−130 °C; ^{1}H NMR 7.45−7.30 (7H, m, H-4, H-5, and 5H−Ar), 6.91−6.88 (2H, m, H-6 and H-8), 5.11 (2H, s, CH_2), 2.17 (3H, s, CH_3); IR (cm^{-1}) 1706, 1611, 1250. Anal. ($C_{17}H_{14}O_3$) C, H.

7-(3-Chlorobenzyloxy)-3-methyl-2*H*-chromen-2-one (43). 57% yield; mp 128−29 °C; ^{1}H NMR 7.44 (2H, d, J = 5.8 Hz, 2H−Ar), 7.34−7.30 (4H, m, H-4, H-5, and 2H−Ar), 6.89 (1H, dd, J = 8.5, 2.5 Hz, H-6), 6.85 (1H, d, J = 2.5 Hz, H-8), 5.08 (2H, s, CH_2), 2.18 (3H, d, J = 1.4 Hz, CH_3); IR (cm^{-1}) 1718, 1622, 1254. Anal. ($C_{17}H_{13}ClO_3$) C, H.

7-Benzenesulfonyloxy-2*H*-chromen-2-one (15). An amount of 1.0 mmol of 7-hydroxycoumarin **1** (162 mg) was dissolved in 5 mL of anhydrous pyridine, and an amount of 3.0 mmol (530 mg, 383 μL) of benzenesulfonyl chloride was added. The mixture was refluxed for 30 min, then poured into ice and acidified with diluted HCl, and the precipitate collected: 98% yield; mp 134−135 °C, from ethanol; ^{1}H NMR 7.85 (2H, d, J = 7.4 Hz, 2H−Ar), 7.70 (1H, t, J = 7.4 Hz, H−Ar), 7.64 (1H, d, J = 9.5 Hz, H-4), 7.55 (2H, t, J = 7.8 Hz, 2H−Ar), 7.42 (1H, d, J = 8.4 Hz, H-5), 7.03 (1H, dd, J = 8.4, 2.2 Hz, H-6), 6.86 (1H, d, J = 2.2 Hz, H-8), 6.39 (1H, d, J = 9.5 Hz, H-3); IR (cm^{-1}) 1734, 1378, 1193. Anal. ($C_{15}H_{10}O_5S$) C, H.

Benzoic Acid (2*H*-2-Oxochromen-7-yl)methyl Ester (16). A solution of bromomethylcoumarin **4** and benzoic acid (10 mmol each) and 30 mmol (3.88 g, 5.23 mL) of *N*,*N*-diisopropylethylamine in 20 mL of anhydrous DMF was stirred for 2 h. The mixture was poured into 20 mL of cold 0.1 N HCl, and the product collected by filtration was purified by crystallization: 88% yield; mp 116−117 °C, from ethanol; ^{1}H NMR 8.09 (2H, dd, J = 7.9, 1.2 Hz, 2H−Ar), 7.71 (1H, d, J = 9.6 Hz, H-4), 7.60 (1H, t, J = 7.4 Hz, H−Ar), 7.51−7.47 (3H, m, H-5 and 2H−Ar), 7.43 (1H, s, H-8), 7.34 (1H, d, J = 8.0 Hz, H-6), 6.43 (1H, d, J = 9.6 Hz, H-3), 5.45 (2H, s, CH_2); IR (cm^{-1}) 1725, 1626, 1286, 1116. Anal. ($C_{17}H_{12}O_4$) C, H.

3,4-Dimethyl-7-(2-phenylethyl)-2*H*-chromen-2-one (17). An amount of 1.0 mmol (292 mg) of *trans*-styryl derivative **18**,[19] dissolved in 5 mL of ethyl acetate, was hydrogenated under atmospheric pressure for 6 h over activated platinum on carbon (10%). After filtration and evaporation of the solvent, a solid was obtained in quantitative yield: mp 119−120 °C, from chloroform/*n*-hexane; ^{1}H NMR 7.49 (1H, d, J = 8.0 Hz, H-5), 7.30−7.06 (7H, m, H-6, H-8, and 5H−Ar), 3.02−2.93 (4H, m, CH_2-CH_2), 2.39 (3H, s, CH_3-4), 2.21 (3H, s, CH_3-3); IR (cm^{-1}) 1704, 1614, 1095. Anal. ($C_{19}H_{18}O_3$) C, H.

7-Benzylthio-3,4-dimethyl-2*H*-chromen-2-one (21). An amount of 3.0 mmol of 7-aminocoumarin **3** (567 mg) was suspended in 21 mL of 10% HCl at −5 °C. An amount of 3.0 mmol (207 mg) of sodium nitrite was then added, followed after 10 min by benzyl mercaptane sodium salt (9.0 mmol, 1.31 g). The mixture was allowed to warm to room temperature and extracted with chloroform. The organic layers, after being washed with water and drying over Na_2SO_4, were evaporated to dryness to give a red oil, which was purified by flash column chromatography with chloroform/petroleum ether (2:8 v/v) as eluent: 25% yield; mp 120−121 °C, from ethyl ether; ^{1}H NMR 7.43 (1H, d, J = 8.4 Hz, H-5), 7.36−7.21 (5H, m, 5H−Ar), 7.16 (1H, d, J = 1.8 Hz, H-8), 7.13 (1H, dd, J = 8.4, 1.8 Hz, H-6), 4.18 (2H, s, CH_2), 2.34 (3H, s, CH_3-4), 2.18 (3H, s, CH_3-3); IR (cm^{-1}) 1703, 1598, 1081. Anal. ($C_{18}H_{16}O_2S$) C, H.

7-Benzylsulfonyl-3,4-dimethyl-2*H*-chromen-2-one (22). An amount of 0.3 mmol of **21** (89 mg) was dissolved under magnetic stirring in 2 mL of acetic acid and heated to 50 °C. An amount of 5 mL of a 3% water solution of $KMnO_4$ was added dropwise within 5 h. After the mixture was cooled, the excess oxidant was decomposed with sodium bisulfite and the solution was diluted with 10 mL of water and extracted with chloroform. The organic layers were collected, washed with a solution of Na_2CO_3 and with water, dried over Na_2SO_4, and evaporated to dryness, giving a crude product that was purified by flash column chromatography using chloroform as eluent: 48% yield; mp 238−240 °C (dec); ^{1}H NMR 7.63 (1H, d, J = 8.3 Hz, H-5), 7.52 (1H, d, J = 1.8 Hz, H-8), 7.47 (1H, dd, J = 8.3, 1.8 Hz, H-6), 7.34−7.22 (3H, m, 3H−Ar), 7.09−7.07 (2H, m, 2H−Ar), 4.34 (2H, s, CH_2), 2.41 (3H, s, CH_3-4), 2.25 (3H, s, CH_3-3); IR (cm^{-1}) 1706, 1144, 1096. Anal. ($C_{18}H_{16}O_4S$) C, H.

***N*-(3,4-Dimethyl-2*H*-2-oxochromen-7-yl)-*N*,4-dimethylbenzenesulfonamide (27).** *N*-(3,4-Dimethyl-2*H*-2-oxochromen-7-yl)-4-methylbenzensulfonamide[19] and sodium hydride (each 0.3 mmol) were dissolved in 3 mL of anhydrous DMF. An amount of 1.0 mmol of

methyl iodide (142 mg, 62 μL) was added, and the mixture was heated at 40 °C for 4 h. The resulting suspension was poured into ice, and the precipitate was collected and crystallized: 83% yield; mp 148−149 °C, from ethanol; ^{1}H NMR 7.54 (1H, d, J = 8.7 Hz, H-5), 7.41−7.39 (2H, m, 2H−Ar), 7.28 (1H, dd, J = 8.7, 2.2 Hz, H-6), 7.24−7.21 (2H, m, 2H−Ar), 6.82 (1H, d, J = 2.2 Hz, H-8), 3.16 (3H, s, N−CH_3), 2.40 (3H, s, CH_3−Ar), 2.38 (3H, s, CH_3-4), 2.27 (3H, s, CH_3-3); IR (cm^{-1}) 1708, 1613, 1348, 1168. Anal. ($C_{19}H_{19}NO_4S$) C, H, N.

3,4-Dimethyl-7-phenoxy-2*H*-chromen-2-one (29). According to the classical von Pechmann procedure,[46] a solution of 3-phenoxyphenol (8 mmol, 1.49 g), ethyl 2-methylacetoacetate (20 mmol, 2.88 g, 2.83 mL), and a few drops of concentrated sulfuric acid was kept at 120 °C for 7 h. The reaction mixture was poured onto ice and extracted with ethyl acetate. The solvent was dried over Na_2SO_4 and eliminated under vacuum, and the residue was purified by column flash chromatography using chloroform/*n*-hexane (6:4 v/v) as eluent: 40% yield; mp 180−181 °C, from ethyl ether/*n*-hexane; ^{1}H NMR 7.54 (1H, d, J = 8.8 Hz, H-5), 7.40 (2H, t, J = 7.4 Hz, H-3′ and H-5′), 7.21 (1H, t, J = 7.4 Hz, H-4′), 7.07 (2H, d, J = 7.4 Hz, H-2′ and H-6′), 6.93 (1H, dd, J = 8.8, 2.5 Hz, H-6), 6.85 (1H, d, J = 2.5 Hz, H-8), 2.39 (3H, s, CH_3-4), 2.20 (3H, s, CH_3-3); IR (cm^{-1}) 1699, 1612, 1085. Anal. ($C_{17}H_{14}O_3$) C, H.

7-(2-Hydroxy-2-phenylethyloxy)-3,4-dimethyl-2*H*-chromen-2-one (31). To a solution of 0.75 mmol (234 mg) of phenone **30**[19] in 15 mL of anhydrous THF, an amount of 38 mg of lithium aluminum hydride (1.0 mmol) was added in small portions, within 2 h, under magnetic stirring at 40 °C. The suspension was cooled to room temperature, the excess of hydride cautiously decomposed with ethyl acetate, the insoluble residue was filtered off, and the solution was evaporated to dryness to afford a solid product in quantitative yield: mp 129−130 °C, from ethanol; ^{1}H NMR 7.48 (1H, d, J = 8.8 Hz, H-5), 7.46−7.31 (5H, m, 5H−Ar), 6.86 (1H, dd, J = 8.8, 2.4 Hz, H-6), 6.79 (1H, d, J = 2.4 Hz, H-8), 5.14 (1H, d, J = 8.1 Hz, *CH*−OH), 4.16−4.04 (2H, m, CH_2−O), 2.68 (1H, d, J = 2.3 Hz, OH), 2.35 (3H, s, CH_3-4), 2.17 (3H, s, CH_3-3); IR (cm^{-1}) 3390, 1695, 1612. Anal. ($C_{19}H_{18}O_4$) C, H.

Optical Resolution of the Racemic Mixture of 31. Pure enantiomers of the racemic mixture of **31** were obtained by semipreparative enantioseparation on a Chiralcel OD HPLC column (250 mm × 4.6 mm i.d.), using *n*-hexane/ethanol (80:20 v/v) as eluent (flow rate 1.0 mL/min; 20 °C; UV monitoring at 320 nm). The first eluted compound (t_R = 19.5 min) corresponded to the (−)-enantiomer, the second one (t_R = 23.5 min) to the (+)-enantiomer. Measurement of specific rotation $[\alpha]_D$ was made with a Perkin-Elmer 341 polarimeter in a 1 dm cell at 20 °C at a concentration of 1 g in 10 mL of $CHCl_3$ and gave values of +30° and −30° for the two optical antipodes.

Synthesis of 3,4-Dimethylcoumarin Derivatives 33, 36, and 37. Title compounds were prepared from 7-hydroxy-3,4-dimethylcoumarin (**2**), the appropriate bromoalkyl derivative, and potassium carbonate (each 10 mmol) in 10 mL of anhydrous DMF by heating at 120 °C for 1−4 h. After cooling, the mixture was poured onto ice. Compound **36** was extracted with chloroform and purified by flash column chromatography using chloroform/ethyl acetate 95:5 (v/v) as eluent. Compounds **33** and **37** were collected as precipitate and recrystallized.

3,4-Dimethyl-7-(2-phenoxyethoxy)-2*H*-chromen-2-one (33). 98% yield; mp 176−177 °C from ethanol; ^{1}H NMR 7.51 (1H, d, J = 8.8 Hz, H-5), 7.33−6.86 (7H, m, H-6, H-8 and 5H−Ar), 4.39−4.34 (4H, m, CH_2−CH_2), 2.37 (3H, s, CH_3-4), 2.19 (3H, s, CH_3-3); IR (cm^{-1}) 1698, 1607, 1235, 1083. Anal. ($C_{19}H_{18}O_4$) C, H.

7-(Benzenesulfonylmethoxy)-3,4-dimethyl-2*H*-chromen-2-one (36). 48% yield; mp 169−170 °C; ^{1}H NMR (DMSO-d_6) 7.91 (2H, d, J = 7.3 Hz, 2H−Ar), 7.76 (1H, t, J = 7.3 Hz, H−Ar), 7.68−7.63 (3H, m, H-5 and 2H−Ar), 7.09 (1H, d, J = 2.5 Hz, H-8), 6.99 (1H, dd, J = 8.8, 2.5 Hz, H-6), 5.70 (2H, s, CH_2), 2.34 (3H, s, CH_3-4), 2.05 (3H, s, CH_3-3); IR (cm^{-1}) 1699, 1612, 1144. Anal. ($C_{18}H_{16}O_5S$) C, H.

7-(3-Phenylprop-2-en-1-yloxy)-3,4-dimethyl-2*H*-chromen-2-one (37). 50% yield; mp 142−143 °C from ethanol; ^{1}H NMR 7.51 (1H, d, J = 8.5 Hz, H-5), 7.47−7.29 (5H, m, 5H−Ar), 6.93−6.74 (3H, m, H-8, H-6, and Ar−*CH*═CH), 6.40 (1H, dt, J = 15,7, 6.3 Hz, Ar−CH═*CH*), 4.75 (2H, d, J = 5.8 Hz, CH−CH_2), 2.38 (3H, s, CH_3-4), 2.19 (3H, s, CH_3-3); IR (cm^{-1}) 1698, 1611, 1174, 1090. Anal. ($C_{20}H_{18}O_3$) C, H.

Computational Methods. Computational analyses were conducted on a 16-node Linux cluster employing an openMosix architecture composed by AMD Athlon XP 2400$^+$ and Intel Xeon 2600 cpu$_s$. Molecules and models were displayed and manipulated on a Silicon Graphics O2+ machine.

CoMFA-GOLPE. Inhibitor molecules were built from the SYBYL fragment libraries.[25] Geometrical optimization and charge calculation were made by means of a quantum mechanical method with the PM3 Hamiltonian. Conformational analysis and molecular overlays were performed according to the procedures and methods described previously.[19,20] Default settings were used in CoMFA, except for the "drop-electrostatic" option, which was set to "NO". The steric and electrostatic interaction energies were calculated at grid points at a regularly spaced 3D lattice with an sp^3 carbon probe atom having a charge of +1 and a van der Waals radius of 1.52 Å. The grid size had a resolution of 1.00 Å, and the region dimensions were defined setting the molecular volume automatic mode in standard CoMFA. Molecular steric, electrostatic, and lipophilic interaction fields were imported into GOLPE,[28] an advanced statistic tool for both variable selection and model validation. The matrix was pretreated by zeroing those data with absolute values smaller than 0.1 kcal/mol and removing any variable with standard deviation below 0.1.

For the derivation of 3D QSAR models, PLS analyses were performed with the "leave-one-out" cross-validation procedure.[27] The optimal number of components (ONC) in the PLS models was considered as the one yielding the smallest standard deviation of error predictions (SDEP) given that the increase of q^2 was not higher than 5% by adding a further component. For an easy comparison of the fitting and predictive power of PLS models, statistics relative to two-component models were also reported in footnotes of Tables 2 and 4. The Smart Region Definition (SRD) algorithm was used to group variables (number of seeds = 1500, critical distance = 1.0 Å, collapsing cutoff = 2.0 Å) and two Fractional Factorial Design (FFD) variable selection runs then followed.

Homology Modeling. The 3D model of the rMAO-B (entry name of AOFB_RAT; primary accession number of P19643 at the ExPASy proteomics server) was developed starting from the X-ray structure of the hMAO-B (PDB code: 1OJC). The two allotropic (homologues) enzymes presented highly close amino acid sequences (519aa vs 520aa, 88.6% of sequence identity) and almost identical amino acid residues in the binding site where the only difference was the substitution of I316 in human by V316 in rat. The spatial model of rMAO-B was constructed through homology modeling[47] within Modeller (version 8.1)[29] after performing sequence alignment with standard options of Clustal_X (version 1.83).[30] Among the 10 best solutions derived from Modeller, the one provided with the lowest value of the Modeller objective scoring function was selected for the subsequent docking simulations. The stereochemical quality of this model, as well as the overall residue-by-residue geometry, was controlled with Procheck (version 3.5.4). When the resolution was set at 2.0 Å, the Ramachandran plot returned 94.4% of residues in the core regions that represent the most favorable combinations of $\varphi-\psi$ angle values and the remaining 5.6% of residues in diverse, but still energetically allowed, regions.[48] Interestingly, the 3D structure of our model was in perfect agreement with the model returned by the SWISS-MODEL, the well-known automated protein homology modeling server, to which the rMAO-B primary sequence was electronically submitted.[49] The interested reader is referred elsewhere for a deeper overview of all the above-mentioned procedures.[50] As expected, the fitting of the α carbons of the binding site residues of theoretical (rMAO-B) and experimental (hMAO-B) models gave a very low deviation (rms = 0.0056 Å), indicating a substantial conservation of their spatial position.

Docking Simulations. GOLD, a genetic algorithm-based software,[31] was used for a docking study selecting GOLDScore as a fitness function. GOLDScore is made up of four components that account for protein−ligand binding energy: protein−ligand hydrogen bond energy (external H-bond), protein−ligand van der Waals energy (external vdw), ligand internal vdw energy (internal vdw), and ligand torsional strain energy (internal torsion). Parameters used in the fitness function (hydrogen bond energies, atom radii and polarizabilities, torsion potentials, hydrogen bond directionalities, and so forth) are taken from the GOLD parameter file. The fitness score is taken as the negative of the sum of the energy terms, so larger fitness scores indicated better bindings. The fitness function has been optimized for the prediction of ligand binding positions rather than the prediction of binding affinities, although some correlation with the latter can be also found.[37] The protein input file may be the entire protein structure or a part of it comprising only the residues that are in the region of the ligand binding site. In the present study, GOLD was allowed to calculate interaction energies within a sphere of a 12 Å radius centered on phenolic oxygen atom of Y435 and Y444 in rMAO-B and rMAO-A, respectively. In some docking runs, as indicated previously, the following physical constraints were set: (i) between the carbamoyl nitrogen atom of Q206 (MAO-B) and the oxygen atom at position 1 of the coumarin ring; (ii) between the oxygen atom of Y435 (MAO-B) and the carbon atom at position 4 of the coumarin ring; (iii) between the β-carbon atom of L167 (MAO-B) and the atom at position 3 of the phenyl ring; (iv) between the oxygen atom of the ether bridge of **9** and phenolic group of Y326.

GRID Analysis. GRID collects a number of different chemical probes for measuring molecular interaction fields.[38] In the present work, a water chemical probe was used to identify favorable locations of functional water molecules within the homology model of rMAO-B. A cube of 28 Å side, centered on the Y435 with a grid size of 0.25 Å (NPLA = 4), was used to calculate the interaction energies. A cutoff of −9 kcal/mol (the most negative energy value was −16.90 kcal/mol) allowed us to intercept four water molecules corresponding to WAT23, WAT82, WAT102, and WAT160 in the 1OJC hMAO-B crystal structure. The rMAO-B including these four water molecules was subsequently used for an additional docking run. The resulting best docked complex, subjected to GRID, yielded a value of −17.41 kcal/mol for the most negative interaction energy. A lower cutoff (−5.5 kcal/mol) was necessary to locate water molecules in the proximity of the ether bridge of **9** (see text).

Biological Assays. MAO inhibitory activity of compounds in Table 1 was assessed using a continuous spectrophotometric assay,[51] monitoring the rate of oxidation of the nonselective nonfluorescent MAO substrate kynuramine to 4-hydroxyquinoline. Briefly, male Sprague-Dawley rats (200−250 g) were sacrificed by decapitation. The brains were immediately removed and washed in an ice-cold isotonic Na_2HPO_4/KH_2PO_4 buffer (pH 7.40) containing sucrose. A crude brain mitochondrial fraction was then prepared by differential centrifugation[52] and stored at −40 °C in an isotonic Na_2HPO_4/KH_2PO_4 buffer (pH 7.4) containing KCl. MAO-A and MAO-B activities in mitochondrial preparations (1 mg/mL) were assayed using as selective and irreversible inhibitors (−)-L-deprenyl (250 nM) and clorgyline (250 nM), respectively. After a preincubation for 5 min with the assayed compound dissolved in DMSO at a final concentration of 5% (v/v), kynuramine was added at a concentration equal to the corresponding K_M value (90 μM for MAO-A and 60 μM for MAO-B). Then the rate of formation of 4-hydroxyquinoline was monitored at 314 nm for 5 min. Finally, IC_{50} values were determined by nonlinear regression of MAO inhibition vs −log of the concentration plots, using the program Origin, version 6.0 (Microcal Software Inc., Northampton, MA).

Acknowledgment. The Spanish authors gratefully acknowledge the financial support of the Ministerio de Ciencia y Tecnologia (Grant BFI2003-00493) and the contribution from the ERDF (Madrid, Spain). The Italian authors thank MIUR, Rome, for financial support (PRIN Project 2004) and Ph.D. students Leonardo Pisani and Teresa Fabiola Miscioscia for their contributions to the experimental work.

Supporting Information Available: Elemental analyses of target compounds. This material is available free of charge via the Internet at http://pubs.acs.org.

References

(1) Tipton, K. F. Enzymology of monoamine oxidase. *Cell Biochem. Funct.* **1986**, *4*, 79−87.
(2) Geha, R. M.; Rebrin, I.; Chen, K.; Shih, J. C. Substrate and inhibitor specificities for human monoamine oxidase A and B are influenced by a single amino acid. *J. Biol. Chem.* **2001**, *276*, 9877−9882.
(3) Johnston, J. P. Some observation upon a new inhibitor of monoamine oxidase in brain tissue. *Biochem. Pharmacol.* **1968**, *17*, 1285−1297.
(4) Grimsby, J.; Lan, N. C.; Neve, R.; Chen, K.; Shih, J. C. Tissue distribution of human monoamine oxidase-A and oxidase-B messenger-Rna. *J. Neurochem.* **1990**, *55*, 1166−1169.
(5) Fowler, C. J.; Ross, S. B. Selective inhibitors of monoamine oxidase A and B: biochemical, pharmacological and clinical properties. *Med. Res. Rev.* **1984**, *4*, 323−358.
(6) Yamada, M.; Yasuhara, H. Clinical pharmacology of MAO inhibitors: Safety and future. *Neurotoxicology* **2004**, *25*, 215−221.
(7) Kyburz, E. New developments in the field of MAO inhibitors. *Drug News Perspect.* **1990**, *3*, 592−599.
(8) Drukarch, B.; van Muiswinkel, F. L. Drug treatment of Parkinson's disease. Time for phase II. *Biochem. Pharmacol.* **2000**, *59*, 1023−1031.
(9) Riederer, P.; Danielczyk, W.; Grunblatt, E. Monoamine oxidase-B inhibition in Alzheimer's disease. *Neurotoxicology* **2004**, *25*, 271−277.
(10) (a) Binda, C.; Newton-Vinson, P.; Hubalek, F.; Edmondson, D. E.; Mattevi, A. Structure of human monoamine oxidase B, a drug target for the treatment of neurological disorders. *Nat. Struct. Biol.* **2002**, *9*, 22−26. (b) Binda, C.; Li, M.; Hubalek, F.; Restelli, N.; Edmondson, D. E.; Mattevi, A. Insights into the mode of inhibition of human mitochondrial monoamine oxidase B from high-resolution crystal structures. *Proc. Natl. Acad. Sci. U.S.A.* **2003**, *100*, 9750−9755.
(11) Ma, J. C.; Yoshimura, M.; Yamashita, E.; Nakagawa, A.; Ito, A.; Tsukihara, T. Structure of rat monoamine oxidase A and its specific recognitions for substrates and inhibitors. *J. Mol. Biol.* **2004**, *338*, 103−114.
(12) De Colibus, L.; Li, M.; Binda, C.; Lustig, A.; Edmondson, D. E.; Mattevi, A. Three-dimensional structure of human monoamine oxidase A (MAO A): Relation to the structures of rat MAO A and human MAO B. *Proc. Natl. Acad. Sci. U.S.A.* **2005**, *102*, 12684−12689.
(13) Novaroli, L.; Reist, M.; Favre, E.; Carotti, A.; Catto, M.; Carrupt, P. A. Human recombinant monoamine oxidase B as reliable and efficient enzyme source for inhibitor screening. *Bioorg. Med. Chem.* **2005**, *13*, 6212−6217.
(14) Geha, R. M.; Chen, K.; Shih, J. C. Phe(208) and Ile(199) in human monoamine oxidase A and B do not determine substrate and inhibitor specificities as in rat. *J. Neurochem.* **2000**, *75*, 1304−1309.
(15) Novaroli, L. Rational strategy and screening methods to identify multifunctional hits for the treatment of PD and AD. Ph.D. Thesis, No. 3643, Université de Genève, Faculté des Sciences, 2005.
(16) Altomare, C.; Carrupt, P. A.; Gaillard, P.; El Tayar, N.; Testa, B.; Carotti, A. Quantitative structure metabolism relationship analyses of Mao-mediated toxication of 1-methyl-4-phenyl-1,2,3,6-tetrahydropyridine and analogs. *Chem. Res. Toxicol.* **1992**, *5*, 366−375.
(17) (a) Kneubuhler, S.; Carta, V.; Altomare, C.; Carotti, A.; Testa, B. Synthesis and monoamine-oxidase inhibitory activity of 3-substituted 5*H*-indeno[1,2-*c*]pyridazines. *Helv. Chim. Acta* **1993**, *76*, 1956−1963. (b) Kneubuhler, S.; Thull, U.; Altomare, C.; Carta, V.; Gaillard, P.; Carrupt, P. A.; Carotti, A.; Testa, B. Inhibition of monoamine oxidase-B by 5*H*-indeno[1,2-*c*]pyridazines. Biological activities, quantitative structure−activity-relationships (QSARs) and 3D-QSARs. *J. Med. Chem.* **1995**, *38*, 3874−3883. (c) Altomare, C.; Cellamare, S.; Summo, L.; Catto, M.; Carotti, A.; Thull, U.; Carrupt, P. A.; Testa, B.; Stoeckli-Evans, H. Inhibition of monoamine oxidase-B by condensed pyridazines and pyrimidines: effects of lipophilicity and structure−activity relationships. *J. Med. Chem.* **1998**, *41*, 3812−3820. (d) Thull, U.; Kneubuhler, S.; Gaillard, P.; Carrupt, P. A.; Testa, B.; Altomare, C.; Carotti, A.; Jenner, P.; Mcnaught, K. S. P. Inhibition of monoamine-oxidase by isoquinoline derivatives. Qualitative and 3D-quantitative structure−activity-relationships. *Biochem. Pharmacol.* **1995**, *50*, 869−877.
(18) Carotti, A.; Carrieri, A.; Chimichi, S.; Boccalini, M.; Cosimelli, B.; Gnerre, C.; Carotti, A.; Carrupt, P. A.; Testa, B. Natural and synthetic geiparvarins are strong and selective MAO-B inhibitors. Synthesis and SAR studies. *Bioorg. Med. Chem. Lett.* **2002**, *12*, 3551−3555.

(19) Gnerre, C.; Catto, M.; Leonetti, F.; Weber, P.; Carrupt, P. A.; Altomare, C.; Carotti, A.; Testa, B. Inhibition of monoamine oxidases by functionalized coumarin derivatives: Biological activities, QSARs, and 3D-QSARs. *J. Med. Chem.* **2000**, *43*, 4747−4758.
(20) Carotti, A.; Altomare, C.; Catto, M.; Gnerre, C.; Summo, L.; De Marco, A.; Rose, S.; Jenner, P.; Testa, B. Lipophilicity plays a major role in modulating monoamine oxidase B (MAO-B) inhibition by 7-substituted coumarins. *Chem. Biodiversity* **2006**, *3*, 134−144.
(21) Bruhlmann, C.; Ooms, F.; Carrupt, P. A.; Testa, B.; Catto, M.; Leonetti, F.; Altomare, C.; Carotti, A. Coumarin derivatives as dual inhibitors of acetylcholinesterase and monoamine oxidase. *J. Med. Chem.* **2001**, *44*, 3195−3198.
(22) Atkins, R. L.; Bliss, D. E. Substituted coumarins and azacoumarins. Synthesis and fluorescent properties. *J. Org. Chem.* **1978**, *43*, 1975−1980.
(23) Rendenbach-Müller, B.; Schlecker, R.; Traut, M.; Weifenbach, H. Synthesis of coumarins as subtype-selective inhibitors of monoamine-oxidase. *Bioorg. Med. Chem. Lett.* **1994**, *4*, 1195−1198.
(24) Cramer, R. D., III; Patterson, D. E.; Bunce, J. D. Comparative molecular field analysis (CoMFA). 1. Effect of shape on binding of steroids to carrier proteins. *J. Am. Chem. Soc.* **1988**, *110*, 5959−5967.
(25) SYBYL, version 7.1; Tripos Inc. (1699 South Hanley Road, St. Louis, MO 63144).
(26) Gaillard, P.; Carrupt, P. A.; Testa, B.; Boudon, A. Molecular lipophilicity potential, a tool in 3D QSAR. Methods and applications. *J. Comput.-Aided Mol. Des.* **1994**, *8*, 83−96.
(27) Dunn, W. J., III; Wold, S.; Edlund, U.; Hellberg, S.; Gasteiger, J. Multivariate structure−activity relationships between data from a battery of biological tests and an ensemble of structure descriptors: the PLS method. *Quant. Struct.-Act. Relat.* **1984**, *3*, 131−137.
(28) Baroni, M.; Costantino, G.; Cruciani, G.; Riganelli, D.; Valigi, R.; Clementi, S. Generating optimal linear PLS estimations (GOLPE): an advanced chemometric tool for handling 3D-QSAR problems. *Quant. Struct.−Act. Relat.* **1993**, *12*, 9−20.
(29) Marti-Renom, M. A.; Stuart, A. C.; Fiser, A.; Sanchez, R.; Melo, F.; Sali, A. Comparative protein structure modelling of genes and genomes. *Annu. Rev. Biophys. Biomol. Struct.* **2000**, *29*, 291−325.
(30) Thompson, J. D.; Gibson, T. J.; Plewniak, F.; Jeanmougin, F.; Higgins, D. G. The CLUSTAL_X windows interface: flexible strategies for multiple sequence alignment aided by quality analysis tools. *Nucleic Acids Res.* **1997**, *24*, 4876−4882.
(31) Jones, G.; Willett, P.; Glen, R. C.; Leach, A. R.; Taylor, R. Development and validation of a genetic algorithm for flexible docking. *J. Mol. Biol.* **1997**, *267*, 727−748.
(32) Schulz-Gasch, T.; Stahl, M. Binding site characteristics in structure-based virtual screening: evaluation of current docking tools. *J. Mol. Model.* **2003**, *9*, 47−57.
(33) Wang, R.; Lu, Y.; Wang, S. Comparative evaluation of 11 scoring functions for molecular docking. *J. Med. Chem.* **2003**, *46*, 2287−2303.
(34) Kellenberger, E.; Rodrigo, J.; Muller, P.; Rognan, D. Comparative evaluation of eight docking tools for docking and virtual screening accuracy. *Proteins: Struct., Funct., Bioinf.* **2004**, *57*, 225−242.
(35) Warren, G. L.; Andrews, C. W.; Capelli, A. M.; Clarke, B.; LaLonde, J.; Lambert, M. H.; Lindvall, M.; Nevins, N.; Semus, S. F.; Senger, S.; Tedesco, G.; Wall, I. D.; Woolven, J. M.; Peishoff, C. E.; Head, M. S. A critical assessment of docking programs and scoring functions. *J. Med. Chem.*, in press.
(36) Westhead, D. R.; Clark, D. E.; Murray, C. W. A comparison of heuristic search algorithms for molecular docking. *J. Comput.-Aided Mol. Des.* **1997**, *11*, 209−228.
(37) Verdonk, M. L.; Cole, J. C.; Hartshorn, M. J.; Murray, C. W.; Taylor, R. D. Improved protein−ligand docking using Gold. *Proteins: Struct., Funct., Bioinf.* **2003**, *52*, 609−623.
(38) Goodford, P. J. A computational procedure for determining energetically favorable binding sites on biologically important macromolecules. *J. Med. Chem.* **1985**, *28*, 849−857.
(39) Reist, M.; et al. Unpublished data.
(40) Carotti, A.; Leonetti, F.; Stefanachi, A.; Catto, M.; Capaldi, C.; Muncipinto, G.; Pisani, L.; Nicolotti, O. In silico design and focused solid phase synthesis of new, selective enzyme inhibitors with potential in cancer and neurological therapies. *Sci. Pharm.* **2005**, *73*, S27.
(41) O'Kennedy, R., Thornes, R. D., Eds. *Coumarins. Biology, Applications and Mode of Action*; John Wiley and Sons: Chichester, U.K., 1997.
(42) Rendenbach, B.; Weifenbach, H. Teschendorf, H.-J. Arylalkoxycumarine. Verfahren zu Ihre Herstellung und Diese Enthalende Therapeutische Mittel (Arylalkoxycoumarins. Their Production Procedures and Therapeutics). Patent DE 3834861 A1, 1990 (BASF AG).
(43) Schlecker, R.; Schmidt, P.; Thieme, P. C.; Lenke, D.; Teschendorf, H. J.; Traut, M.; Müller, C. D.; Hofmann, J. P.; Kreiskott, H. Neue Sulfonsäureester von Hydroxycumarinen, Ihre Herstellung und Sie Enthaltende Arzneimittel (New Sulfonic Acid Esters of Hydroxycoumarins: Their Production and Medicinal Properties). Patent DE 3243158 A1, 1984 (BASF AG).
(44) Ahluwalia, V. K.; Kumar, D.; Gupta, Y. K. Claisen rearrangement of some 7-cinnamyloxybenzo-α-pyrones. *Indian J. Chem.* **1978**, *16B*, 579−583.
(45) Gia, O.; Uriarte, E.; Zagotto, G.; Baccichetti, F.; Antonello, C.; Marcianimagno, S. Synthesis and photobiological activity of new methylpsoralen derivatives. *J. Photochem. Photobiol., B* **1992**, *14*, 95−104.
(46) von Pechmann, H. Duisberg, C. Über die verbindungen der phenole mit acetessigäther (On the compounds of phenol with acetoacetate). *Chem. Ber.* **1883**, *16*, 2119−2128.
(47) Marti-Renom, M. A.; Stuart, A. C.; Fiser, A.; Sanchez, R.; Melo, F.; Sali, A. Comparative protein structure modelling of genes and genomes. *Annu. Rev. Biophys. Biomol. Struct.* **2000**, *29*, 291−325.
(48) Laskowski, R. A.; Macarthur, M. W.; Moss, D. S.; Thornton, J. M. Procheck. A program to check the stereochemical quality of protein structures. *J. Appl. Crystallogr.* **1993**, *26*, 283−291.
(49) Schwede, T.; Kopp, J.; Guex, N.; Peitsch, M. C. SWISS-MODEL: an automated protein homology-modelling server. *Nucleic Acids Res.* **2003**, *31*, 3381−3385.
(50) Lesk, A. M. *Introduction to Protein Science Architecture, Function, and Genomics*; Oxford University Press: Oxford, U.K., 2004.
(51) Mendez-Alvarez, E.; Soto-Otero, R.; Sanchez-Sellero, I.; Lopez-Rivadulla, L. M.; Lamas, M. Inhibition of brain monoamine oxidase by adducts of 1,2,3,4-tetrahydroisoquinoline with components of cigarette smoke. *Life Sci.* **1997**, *60*, 1719−1727.
(52) Soto-Otero, R.; Mendez-Alvarez, E.; Hermida-Ameijeiras, A.; Sanchez-Sellero, I.; Cruz-Landeira, A.; Lamas, M. L. R. Inhibition of brain monoamine oxidase activity by the generation of hydroxyl radicals. Potential implications in relation to oxidative stress. *Life Sci.* **2001**, *69*, 879−889.

JM060183L